# Fractal geometry of contacting patches in rough elastic contacts

Joseph M. Monti<sup>a,\*\*</sup>, Lars Pastewka<sup>b,c</sup>, Mark O. Robbins<sup>a,</sup>

<sup>a</sup> Department of Physics and Astronomy, Johns Hopkins University, 3400 North Charles Street, Baltimore, MD 21218, USA
<sup>b</sup> Department of Microsystems Engineering, University of Freiburg, Georges-Köhler-Allee 103, 79110 Freiburg, Germany
<sup>c</sup> Cluster of Excellence livMatS, Freiburg Center for Interactive Materials and Bioinspired Technologies, University of Freiburg, Georges-Köhler-Allee 105, 79110 Freiburg, Germany

#### Abstract

Many naturally formed and processed surfaces are rough over a broad range of length scales. Surface roughness reduces the area of contact between solids, with ramifications for phenomena that depend on the geometry of the interface and the amount of direct contact, including friction and adhesion. In this work, we employ large-scale boundary-element simulations for nonadhesive, elastic solids to study the size dependence of contact patch mean pressure and geometry for patches formed between solids with self-affine fractal surface roughness across seven decades in patch area. Contact patches with diameters smaller than a crossover length scale of order the minimum wavelength of roughness are generally compact with simple geometries and bear pressures well described by Hertz theory. The patch pressure in contact patches larger than the crossover scale rises logarithmically before saturating at a finite value. Furthermore, the largest contact patches formed during our simulations are ramified and populated with regions out of contact, or bubbles, which reduce patch area and increase patch perimeter. As a result, we show that the mean contact diameter of the largest patches saturates, indicating that the patch contact area is proportional to the total patch perimeter. We quantify the effects of bubbles on patch area and perimeters as a function of Hurst exponent and contrast our findings with results of comparable bearing-area model calculations. The slow evolution of the mean patch pressure with patch size in our large-scale calculations explains the common observation that the global mean contact pressure depends on the structure of the roughness, the contact area, and even on system size.

Keywords: Contact mechanics, Rough surfaces, Friction

### 1. Introduction

The real area of contact between surfaces is critically important in determining the properties and longevity of solid-on-solid interfaces. Friction, adhesion, and wear are sensitive to the total area of close approach between the contacting interfaces, as are the effective thermal conductivity and contact resistance of the contact [1, 2, 3, 4, 5, 6, 7, 8, 9, 10]. Surface roughness generally reduces the contact area far below the apparent or projected surface area  $A_0$  and requires that external load be applied to bring deformable solids closer together after initial contact. Consequently, there has been widespread interest in improving our understanding of how the contact area depends upon roughness structure and applied load.

Experimental, analytical, and numerical studies of rough surfaces commonly find proportionality between the real contact area  $A_{\text{tot}}$  and applied load  $F_{\text{tot}}$  at low contact area fractions [4, 11, 12, 13, 14, 15]. Greenwood and Williamson provided the first plausible explanation for this simple relationship for elastic bodies by assuming that rough surfaces are composed of many identical asperities with radius R, subject to

Email address: jmonti3@jhu.edu (Joseph M. Monti )

<sup>\*</sup>Present address: Sandia National Laboratories, Albuquerque, New Mexico, 87123, USA

<sup>\*\*</sup>Corresponding author.

a rapidly decaying distribution of summit heights [13]. The theory predicted  $A_{\rm tot} \propto F_{\rm tot}$  by summing the independent contributions of contacting asperities behaving in accordance with Hertz theory [16]. Later, Bush et al. extended the Greenwood-Williamson formulation to include a distribution of asperity curvatures [14]. Asperity models such as these provide a useful first approximation of contact behavior but are inherently flawed because they ignore the long-range correlations induced by elastic deformation. More recently, Persson developed a model that included elastic interactions in an approximate way and is exact in the limit of full contact [15, 17]. Bush et al. and Persson both derived expressions of the form  $A_{\rm tot} = \kappa F_{\rm tot}/h'_0 E^*$ , where  $E^*$  is the contact modulus,  $h'_0$  is the root-mean-squared (rms) surface slope and  $\kappa$  is a dimensionless constant that differed slightly between the two models: Bush et al. found  $\kappa = \sqrt{2\pi} \approx 2.5$ , whereas Persson arrived at the value  $\kappa = \sqrt{8/\pi} \approx 1.6$ . The mean pressure in contacting regions,  $p_{\rm rep} \equiv F_{\rm tot}/A_{\rm tot}$ , is written nondimensionally in terms of  $\kappa$  as  $p_{\rm rep}/h'_0 E^* = 1/\kappa$ .

Many natural and processed surfaces exhibit self-affine fractal character over a range of length scales [18, 19, 20]. From a numerical point of view, constructing surfaces with self-affine roughness is a useful way to control the statistical properties of synthetic representations of roughness with just a few parameters. Chiefly, the Hurst exponent H governs height differences between locations on the surface separated by lateral vector  $\vec{r}$ , satisfying  $\langle |h(\vec{x}+\vec{r})-h(\vec{x})|^2 \rangle \propto |\vec{r}|^{2H}$  for isotropic self-affine roughness where the average  $\langle \cdot \rangle$  runs over locations  $\vec{x}$  on the surface. For self-affine fractals, H is between zero and unity with the special limiting case H=1 corresponding to self-similar fractals. Roughness characterized by H=0.5 exhibits a random-walk-like topography and is uncorrelated at small scales, while surfaces with H > 0.5 and H < 0.5are correlated and anti-correlated at short scales, respectively. Measurements of surfaces most often find values of H between 0.5–1 [18, 19, 20, 21]. However, the case of H < 0.5 is also of practical interest as such self-affine roughness has been shown to arise from the Kardar-Parisi-Zhang (KPZ) model [22], in experiments of sputter-deposited Au on Si(111) [23] and ion-beam-eroded graphite [24], and from numerical simulations of plastically deformed amorphous CuZr [25]. Numerical simulations of self-affine rough surfaces have shown that below  $\sim 10\%$  contact percentage  $\kappa$  usually falls between the predictions of Bush et al. and Persson, provided that a statistically representative set of contact patches is formed [26, 27, 28, 29, 30, 31]. However, the precise value of  $\kappa$  depends on the details of surface roughness and is only nominally constant over a limited range of area fractions.

Subtle variations in  $p_{\rm rep}/h_0'E^*$  indicate that probing the mechanisms underlying the evolution of contact area with applied load and changes in roughness is crucial. A regularly reported quantity is the contact patch-size distribution  $n(A_{\rm p})$ , which gives the probability that a connected patch containing area close to  $A_{\rm p}$  exists. Experimentally, Dieterich and Kilgore measured that the patch-size distribution appears to decay as  $n(A_{\rm p}) \sim A_{\rm p}^{-\tau}$  for a variety of roughened materials [11, 12]. The notion of a power-law patch-size distribution is supported by numerous computational studies that have typically found  $\tau < 2$  [6, 32, 33, 34]. One difficulty associated with isolating power-law exponents for  $n(A_{\rm p})$  using simulations is the relatively high computational cost of calculating elastic deformations. Early numerical work was limited to fitting  $\tau$  over merely 1-2 decades of scaling. Moreover, the tails of  $n(A_{\rm p})$  have proved challenging to resolve but  $\tau < 2$  implies that the largest patches dominate the total contact area since  $\int dA_{\rm p} A_{\rm p} n(A_{\rm p}) \sim A_{\rm p}^{-\tau+2}$  has a positive exponent.

Recently, Müser and Wang [34] hypothesized that  $n(A_{\rm p})$  is a truncated power-law distribution with an intrinsic maximum patch size  $A_{\rm max}$ . They found that over a small range,  $\tau$  agreed with the predicted exponents for planar cuts through self-affine surfaces—the so-called bearing-area model—where  $\tau=2-H/2$ . However, their work did not systematically vary the scales of roughness or explore how changes in contact area affected fits to the distribution. We will show that these have significant effects on  $n(A_{\rm p})$ .

Furthermore, the patch-size distribution tells only part of the story for  $p_{\rm rep}/h_0'E^*$  because the applied load is not distributed uniformly over contact patches. The force borne by individual contact patches  $F_{\rm p}$  has previously been studied as a function of  $A_{\rm p}$  [34, 35, 36]. A crossover emerges between Hertz scaling  $F_{\rm p} \sim A_{\rm p}^{3/2}$  for small contacts to linear scaling  $F_{\rm p} \sim A_{\rm p}$  for large patches. By focusing on the mean pressure in patches  $F_{\rm p}/A_{\rm p}$  instead, we will show that the crossover is not sharp but rather takes place gradually over several decades of patch sizes. Most numerical studies to date have employed system sizes unable to produce contact patches large enough to surpass the patch pressure crossover regime, meaning that the largest mean

patch pressure in the system was entirely dictated by the system size. Extrapolations for  $p_{\text{rep}}/h'_0E^*$  based on simulation results obtained for such surfaces with small ranges of self-affine roughness were therefore inapplicable to the limit of broad self-affine roughness.

The morphology of contact patches is widely assumed to be fractal because the synthetic surfaces are fractal themselves [2, 29, 32]. It is possible to define fractal dimensions for both contact patches and the perimeters of patches. A natural basis for comparison to elastic contact geometries is the bearing-area model, for which analytic work has determined fractal dimensions for contour loops generated via planar cuts through Gaussian surfaces [37, 38]. The bearing-area model, like asperity models, ignores correlations between contacting regions mediated by elastic interactions but is nevertheless a useful tool due to its simplicity.

In this paper, we investigate effects of self-affine surface roughness and contact area on  $p_{\rm rep}/h_0'E^*$  for contact area fractions  $A_{\rm tot}/A_0 \lesssim 0.15$  using nonadhesive contact simulations. We observe that the properties of contact patches generally vary systematically with patch size. When possible, we make direct comparisons between elastic calculations and the bearing-area model. Finally, we discuss possible sources of variability for simulation results and explore what our findings imply for the thermodynamic limit of infinite system size.

#### 2. Methods

### 2.1. Rough surface generation

We use a Fourier filtering algorithm to generate instances of randomly rough, periodic surfaces with self-affine power spectral density (PSD) [4, 39]. The roughness is isotropic, meaning that the PSD depends only on the magnitude of the in-plane wavevector  $q = |\vec{q}|$ . The self-affine regime of the PSD is bounded by lower and upper values  $q_1 = 2\pi/\lambda_{\rm max}$  and  $q_2 = 2\pi/\lambda_{\rm min}$ , respectively. The short wavelength cutoff  $\lambda_{\rm min}$  is the length scale below which surfaces are smooth, while the long wavelength cutoff  $\lambda_{\rm max}$  corresponds to the distance beyond which distinct surface regions are statistically independent. The ratio  $\zeta \equiv q_2/q_1 = \lambda_{\rm max}/\lambda_{\rm min}$  defines the extent of self-affinity of the roughness; this is the magnification central to Persson's model [15]. The full PSD is then given by

$$S(q) = \begin{cases} 0 & \text{if } q_1 < q \\ C_0 \left(\frac{q}{q_1}\right)^{-2(1+H)} & \text{if } q_1 \le q \le q_2 \\ C_0 \left(\frac{q_2}{q_1}\right)^{-2(1+H)} & \text{if } q_2 < q \le 2\pi/L \end{cases}$$
 (1)

where L is the overall linear dimension of the periodic rough topography. The prefactor  $C_0$  can be chosen to set one of the moments of the PSD given  $\lambda_{\min}$  and  $\lambda_{\max}$ . Fourier amplitudes in the reciprocal-space surface representation can be chosen to construct surfaces with exact PSDs or by scaling Gaussian random variables to have the correct variance according to Eq. (1). In our simulations, the latter method produced larger variance within the ensemble because of greater variability of the highest peak, but we found that contact results did not strongly depend upon the amplitude-selection method.

For surfaces with broad self-affine regimes  $(\zeta \gg 1)$ ,  $\lambda_{\rm max}$  independently controls the rms height variation  $h_0 = \langle h^2(\vec{x}) \rangle^{1/2}$ , while  $\lambda_{\rm min}$  sets  $h'_0 = \langle |\nabla h|^2 \rangle^{1/2}$  and the rms curvature  $h''_0 = \langle \nabla^2 h \rangle^{1/2}$ . Existing literature often refers to fractal and thermodynamic limits, but often without clearly defining what these limits mean. We here use the following definitions: The fractal limit of self-affine roughness corresponds to  $\zeta \to \infty$  [31], i.e. a broad region of self-affine scaling. The ratio  $L/\lambda_{\rm max}$  determines surface "representativity" [40]: The rough interface is replicated  $(L/\lambda_{\rm max})^2$  times, but in a statistical sense—each repetition has identical statistical properties but does not have identical surface profiles. The thermodynamic limit is then given by  $L/\lambda_{\rm max} \to \infty$  [31]. Surfaces with  $L/\lambda_{\rm max} > 1$  help smooth out measurement fluctuations by permitting self-averaging over statistically independent replicas contained within the system. The resolution of the boundary between contacting and non-contacting regions is governed by  $\lambda_{\rm min}/a_0$ , where  $a_0$  is the surface discretization. In some cases, self-affine roughness has been observed down to the atomic scale [20, 21], but imposing  $\lambda_{\rm min} \gg a_0$  mitigates discretization errors.

The principal length scale of interest for contact patches is  $d_{\rm rep}$ , the characteristic diameter of contacting regions. Pastewka and Robbins expressed  $d_{\rm rep}$  in terms of  $h_0'$  and  $h_0''$  by connecting the latter to the statistical radius of curvature of asperities via  $R_{\rm asp} = 2/h_0''$ , yielding  $d_{\rm rep} = 4h_0'/h_0''$  [2, 41]. Contributions from  $q_1$  can be dropped for  $\zeta \gg 1$  giving:

$$d_{\text{rep}} = \frac{2\lambda_{\min}}{\pi} \sqrt{\frac{2-H}{1-H}}; \quad H < 1.$$
 (2)

Note that this quantity encodes explicit dependence on H, with the narrowest diameters corresponding to small H. We mainly report length scales normalized by  $d_{\text{rep}}$  and area scales normalized by  $d_{\text{rep}}^2$ , computed using Eq. (2).

#### 2.2. Elastic contact mechanics

The problem of frictionless, normal contact of two elastic solids with Young's moduli  $E_1$  and  $E_2$  and Poisson ratios  $\nu_1$  and  $\nu_2$  can be mapped to contact between a rigid body and an elastic body with effective contact modulus given by [42]:

$$\frac{1}{E^*} = \frac{1 - \nu_1^2}{E_1} + \frac{1 - \nu_2^2}{E_2}.\tag{3}$$

A similar mapping exists for combining two rough surfaces because only the undeformed gap function matters for linear elasticity. Statistical moments describing the roughness of the resulting composite surface increase by a factor of  $\sqrt{2}$  as a result of the incoherent sum of the original topographies. We take  $h'_0 = 0.1$  for the combined surface because it is typical of experimentally measured surfaces, and because larger slopes  $h'_0 \approx 1$  often produce plastic deformation in real materials. However, the value of  $h'_0$  is inconsequential in linear elasticity because the natural unit of pressure is  $h'_0E^*$ . We report all pressures normalized by this quantity.

We employ a boundary-element technique to calculate the deformation of semi-infinite, linear elastic solids [43, 44, 45, 46, 47, 48]. The interaction between substrate and rough surface is a hard wall such that there is no interpenetration. Each node has a single degree of freedom to displace perpendicular to the surface plane; nodes on the elastic solid's surface are considered to be in contact where the pressure is positive, and each contacting node contributes  $a_0^2$  to the overall contact area. For periodic systems, the stiffness of the q=0 mode (defining uniform translations of the surface layer) vanishes; therefore, we set the q=0 stiffness equal to the stiffness of the smallest q>0 mode [28, 47, 48].

### 2.3. Corrections to contact area

Yastrebov and coworkers have emphasized the importance of using sufficient resolution to reduce discretization effects, in particular to avoid overestimation of the contact area and to prevent erroneously merging contact patches that should be distinct [30, 49]. In a recent set of papers, they derived the correction:

$$A'_{\text{tot}} = A_{\text{tot}} - \frac{\pi - 1 + \log(2)}{24} P_{\text{tot}} a_0, \tag{4}$$

where  $A_{\rm tot}$  and  $P_{\rm tot}$  are the global contact area and perimeter. The contact area is computed by summing up the areas of contacting nodes, and the perimeter is the total length of edges shared by contacting and non-contacting nodes. In the present work, contact nodes belong to the same patch if they are next-nearest neighbors, meaning that they share an edge or corner on the square grid. For low-resolution calculations ( $\lambda_{\rm min} \lesssim 10a_0$ ), comparing nearest and next-nearest neighboring criteria will likely give slightly different results. We apply Eq. (4) to individual contact patches by replacing  $A_{\rm tot}$  and  $P_{\rm tot}$  with their per-patch analogs  $A_{\rm p}$  and  $P_{\rm p}$ . Results were minimally affected if  $\lambda_{\rm min} \gtrsim 10a_0$ , and in this work, we fix  $\lambda_{\rm min} = 16a_0$  (see Supporting Information of Ref. [2] for more details).

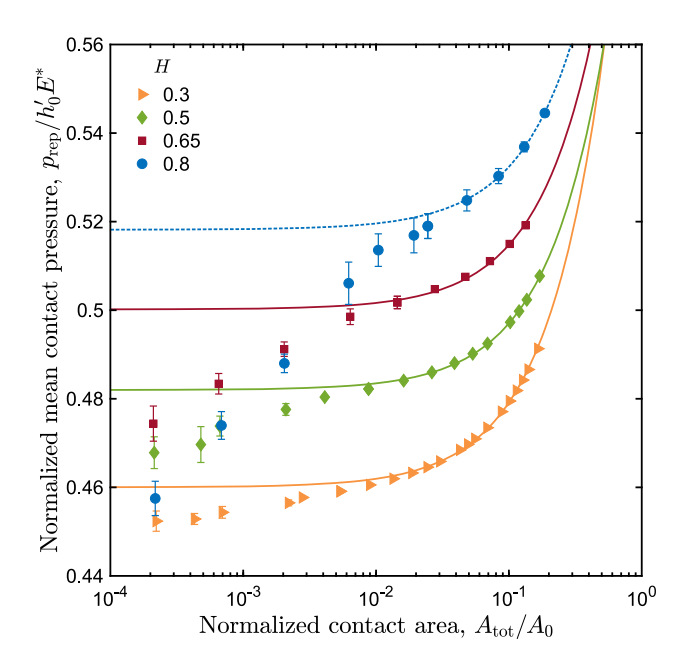


Figure 1: Variation of the dimensionless mean contact pressure  $p_{\rm rep}/h_0'E^*$  with contact area fraction for the indicated H. Error bars represent the standard error on the mean measured across an ensemble of more than ten typical surfaces. Solid lines indicate linear fits to the data with matching colors. The dashed line is a tentative linear fit to the H=0.8 data over the range  $A_{\rm tot}/A_0 \gtrsim 0.04$ . The system side length is  $\lambda_{\rm max}=16384a_0$  and  $\zeta=1024$ .

# 3. Results & Discussion

### 3.1. Pressure in contacting regions

### 3.1.1. Mean pressure in the full contact

Numerical simulations have shown that the mean contact pressure increases steadily with additional load [29, 30, 31, 49, 50]. Figure 1 shows that  $p_{\rm rep}$  varies continuously from low contact percentages corresponding to about  $A_{\rm tot} \sim 10^2 \lambda_{\rm min}^2$  up through the  $10^{-2} \lesssim A_{\rm tot}/A_0 \lesssim 10^{-1}$  contact fraction regime where the mean pressure is often assumed to be constant. The first few asperities to touch strongly dominate initial values of  $p_{\rm rep}$ , resulting in relatively large variation as shown most clearly by the error bar for H=0.8 for  $A_{\rm tot}/A_0 < 0.01$ . The surface height variance grows as  $\zeta^H$ , so relatively few contact patches are present at low area fractions for H>0.5 when  $L=\lambda_{\rm max}$ . As we will show later, the mean pressure in contacts between asperities is independent of H, so the overall mean pressure is similarly insensitive to H in this regime. Once larger contact patches form, in this case for  $A_{\rm tot}/A_0 \gtrsim 10^{-3}$ , mean pressure dependence on H clearly emerges. Given a statistically representative system with large  $L/\lambda_{\rm max}$  and  $\zeta$ , the onset of this small contact patch count behavior shifts to smaller  $A_{\rm tot}/A_0$  (particularly for H>0.5).

Beyond the early contact behavior,  $p_{\rm rep}$  is nearly independent of contact area over a range of areas that broadens as H decreases. Note that  $p_{\rm rep}$  consistently increases with H at fixed area above  $A_{\rm tot}/A_0\approx 0.005$ . We found that fits of the form  $p_{\rm rep}/h_0'E^*=p_0/h_0'E^*+cA_{\rm tot}/A_0$  (solid lines in Fig. 1) worked fairly well in the 0.01-0.20 contact fraction regime for  $H\leq 0.5$  and over a narrower range for H>0.5, suggesting that there may be a unique asymptotic mean pressure in the infinitesimal contact limit for large systems (at finite  $\lambda_{\rm min}/a_0$  [31]). Indeed, the area-independent regime extends to lower area fractions for all H when  $\zeta$  and L grow. Note that we also include a tentative linear fit for our H=0.8 data (dashed blue line), but the agreement for  $A_{\rm tot}/A_0\lesssim 0.01$  is poor.

Figure 2 illustrates the effect of H on  $p_{\rm rep}$  more clearly for three different applied loads. The mean pressure generally lies around  $0.5h_0'E^*$  or  $\kappa\approx 2$  even at very low area fractions. The increase in mean pressure at fixed applied load results from the real contact area falling with H. Note that tenfold and

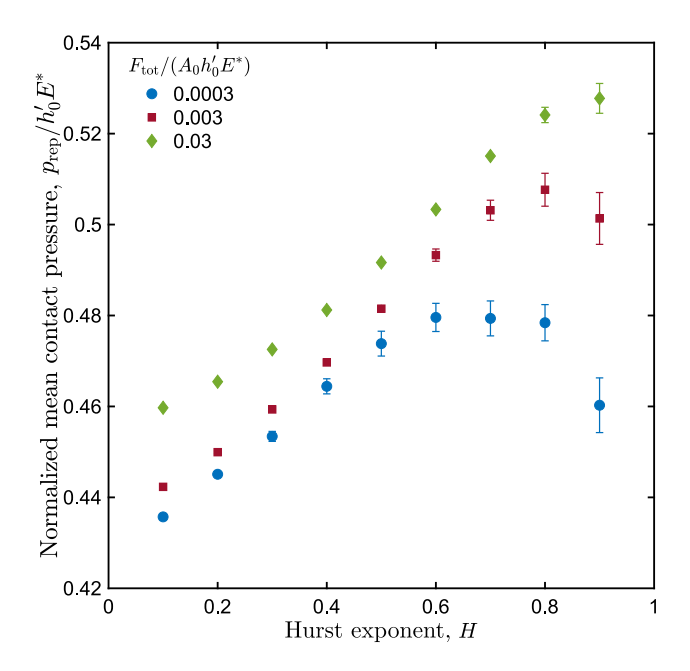


Figure 2: Systematic variation of  $p_{\rm rep}/h_0'E^*$  with H at the indicated applied loads roughly corresponding to 0.06% (blue), 0.6% (red) and 6% (green) contact percentage. Error bars represent the standard error on the mean. The system side length is  $16384a_0$  and  $\zeta = 1024$ .

hundredfold increases in the applied load produced small upward shifts in the mean pressure, signifying that in all cases the total contact area grew by slightly less than the same factors as the load. Above  $A_{\rm tot}/A_0\approx 0.01,\ p_{\rm rep}$  grows monotonically with H, but at smaller area fractions the dependence is non-monotonic. This behavior is sensitive to L and  $\zeta$  but we fix both here to focus on the effect of varying H. A wider spread of  $p_{\rm rep}$  within the ensemble is evident for H>0.5 and is reflected by the error bars in Fig. 2.

At  $A_{\rm tot}/A_0 \approx 0.06$ , data for  $H \to 0$  lie near to the prediction of Bush et al., i.e.,  $p_{\rm rep}/h'_0 E^* = \kappa^{-1} \approx 0.4$ , whereas as H increases values of  $p_{\rm rep}/h'_0 E^*$  are closer to the value computed from Persson's model,  $\kappa^{-1} \approx 0.63$ . A possible simple explanation for the systematic change between limiting numerical values relies on observations from earlier work [5, 35, 39] that showed that the contact autocorrelation function measured above the background decays as  $\Delta C_c(r) \propto r^{-|H-1|}$  or, equivalently, that its Fourier transform  $\tilde{C}_c(q) \sim q^{-(1+H)}$  (we verified this result for our own computations). Since the autocorrelation function falls with the distance between contact patches most rapidly for  $H \to 0$ , elastic correlations are less important for small H at large length scales. The opposite is true for  $H \to 1$ , where contact correlations persist to large length scales.

A wide variety of computational techniques have been used in numerical studies of the contact of rough surfaces [4, 28, 30]. These studies were usually limited to system sizes with side lengths of a few thousand nodes and total degrees of freedom numbering in the millions to tens of millions. While this is sufficient for making general statements about trends and approximating contact distributions, it is difficult to determine conclusively which contact quantities are fully resolved. For example, analysis by Yastrebov et al. suggested that  $\kappa$  decreases logarithmically with Nayak's parameter  $\alpha$ , which scales as  $\alpha \sim \zeta^{2H}$  for large  $\zeta$  [31, 50, 51]. The authors hypothesized that the trend would continue in the fractal limit for all H, implying that  $p_{\rm rep}$  should diverge at fixed fractional contact area for large systems. Our simulations produced results, shown in Fig. 3, that invalidate this prediction (see also Ref. [31] for additional discussion on this issue). For H < 0.5, we find that  $p_{\rm rep}$  saturates rather quickly with respect to  $\zeta$  at fixed load, i.e. above  $\zeta > 300$  or  $\alpha > 100$ . Conversely, there is significant dependence on  $\zeta$  for H > 0.5; by  $\zeta = 4096$  for H = 0.8,  $p_{\rm rep}/h'_0E^*$  is only beginning to saturate to a plateau. It is possible that  $\zeta > 10^4$  or  $\alpha > 10^5$  is necessary to confirm the plateau value. We note that similar trends were observed in Ref. [31] (see Fig. 6). We include data for H = 0.5

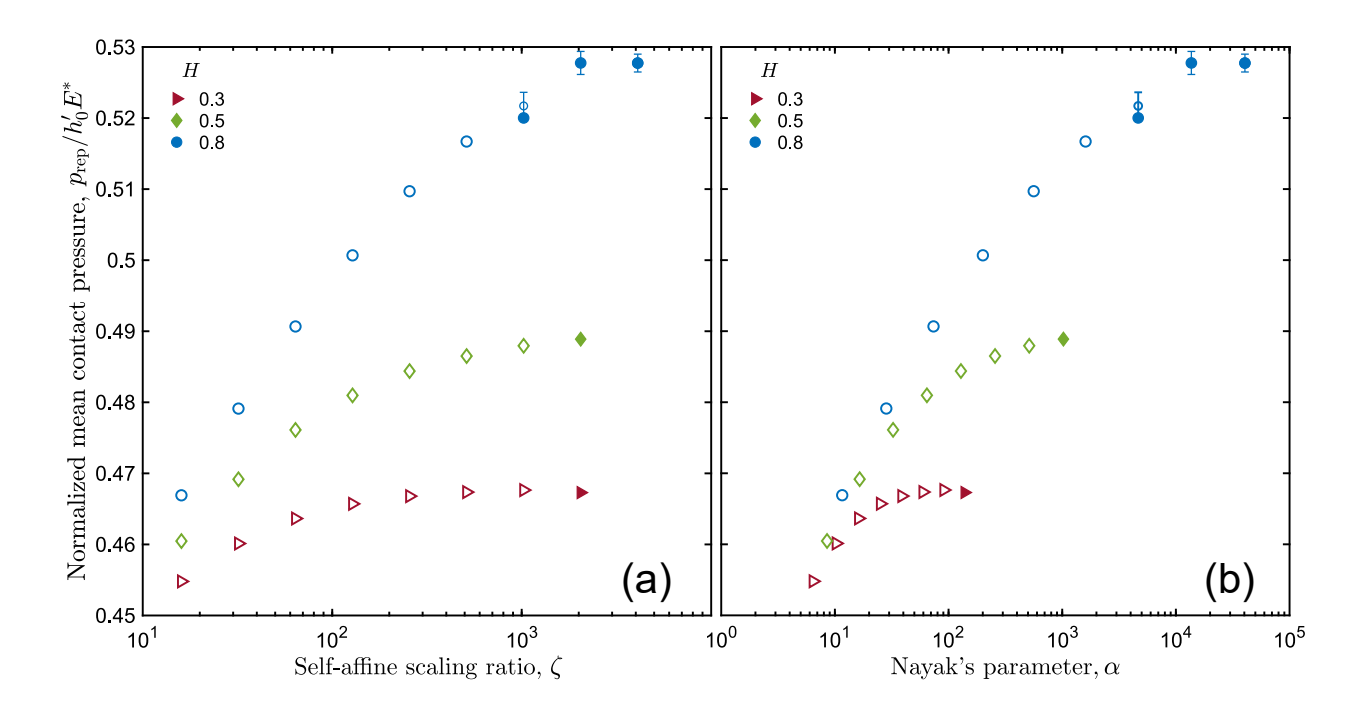


Figure 3: (a): Variation of  $p_{\rm rep}/h_0'E^*$  with  $\zeta$ . Error bars are plotted when the error magnitude is larger than the marker size and represent the standard error on the mean.  $L=16384a_0$  for open symbols. For filled symbols,  $L=65536a_0$  for H=0.8 and H=0.5. (b): The same data as in panel (a), but plotted against Nayak's parameter,  $\alpha$ .

to show that the fractal limit gradually moves to larger  $\zeta$  with increasing H. Most previous computational work has focused on  $\zeta$  smaller than shown in Fig. 3 out of computational necessity and therefore cannot be considered to be in the fractal limit.

### 3.1.2. Mean pressure in individual contact patches

The preceding results have demonstrated that  $p_{\text{rep}}$  depends on roughness structure in a complicated way, but it is difficult to find a satisfactory explanation for this dependence by only considering collectivelymeasured quantities. To address this challenge, we note that  $p_{\text{rep}}$  is an area-weighted sum of the mean pressures  $p_p = F_p/A_p$  within individual contact patches. As discussed previously,  $F_p$  has been the focus of several studies but  $p_p$  provides more insight into the crossover regime. Figure 4 shows that similar to  $F_{\rm p}$  [34, 36],  $p_{\rm p}$  also divides contact patches into two branches. The small contact patch-size branch contains patches with areas of order  $d_{\rm rep}^2$  or smaller and exhibits a  $p_{\rm p} \sim \sqrt{A_{\rm p}}$  scaling consistent with Hertz theory (Fig. 4 inset). Contact patches in this regime are produced by asperities with radii well approximated by  $R_{\rm asp} \sim d_{\rm rep}/h'_0$ , and patch pressure data for different H collapse because  $d_{\rm rep}$  encodes the dependence on H. The constraint that  $\lambda_{\min} > 10a_0$  amounts to a criterion for simulations to be able to resolve the variation in pressure across the contact diameter and is linked with Persson's prediction that the pressure distribution vanishes linearly at low pressures [15, 17, 33]. We checked that the mean pressure in small patches continues to follow Hertz scaling up to  $\lambda_{\min} = 256a_0$  (Fig. 4 inset). The numerical discretization becomes increasingly important for small patches as  $\lambda_{\min}$  decreases and the mean pressure in the smallest patches with size  $A_{\rm p} \approx a_0^2$  is always overvalued. However, the fraction of the total load carried by patches in the Hertz branch of Fig. 4 is small for all H.

Hertz scaling breaks down once the patch size approaches  $d_{\text{rep}}^2$ , with the greatest fidelity evident for H=0.3. Figure 4 shows that  $p_{\text{p}}$  undergoes a sharp transition away from Hertz scaling in the vicinity of  $A_{\text{p}}/d_{\text{rep}}^2 \approx 0.1$  for each H. Rather than remaining constant,  $p_{\text{p}}$  continues to rise with increasing  $A_{\text{p}}$  in a manner that may be best described as logarithmically, with a rate of increase that grows with H. The onset of the logarithmic regime moves to smaller  $A_{\text{p}}/d_{\text{rep}}^2$  as H rises and there is a corresponding drop in the

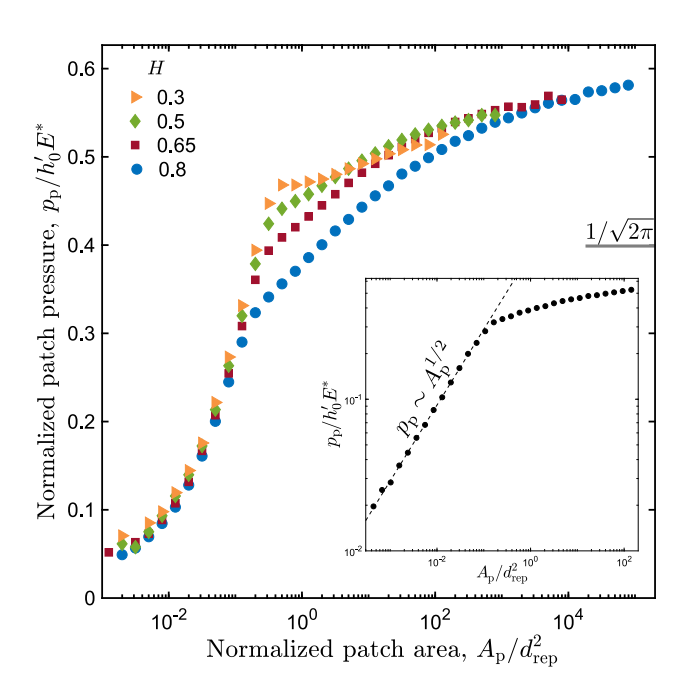


Figure 4: Dimensionless mean pressure within contact patches as a function of patch size for the indicated H at  $A_{\rm tot}/A_0\approx 0.05$ . For H=0.3 and H=0.5,  $L=32768a_0$  and  $\zeta=2048$ . For H=0.65 and H=0.8,  $L=65536a_0$  and  $\zeta=4096$ . The upper bound of the figure corresponds to Persson's prediction  $p_{\rm rep}/h_0'E^*=\kappa^{-1}=\sqrt{\pi/8}$ . The thin gray line marks the prediction of Bush et al.  $\kappa^{-1}=1/\sqrt{2\pi}$ . Inset: Log-log axis representation of the  $p_{\rm p}\sim A_{\rm p}^{1/2}$  scaling of the mean patch pressure for small patches for a surface with H=0.8,  $\lambda_{\rm max}=L=65536a_0$ , and  $\lambda_{\rm min}=256a_0$ . The dashed black line is a fit to the data and has power-law exponent 1/2.

maximum  $p_{\rm p}$  attained in the Hertz branch. An interesting consequence of the log-like growth of  $p_{\rm p}$  is that the mean pressures in large patches (i.e.  $A_{\rm p}\gtrsim 10^2 d_{\rm rep}^2$ ) are similar for all values of H.

Of course, the ability to compute  $p_{\rm p}$  for progressively larger patches is contingent on those patches being present. Figure 4 indirectly shows the maximum patch size we observed for each H, which plainly grows with H. Our simulations show that the logarithmic regime persists for several decades of  $A_{\rm p}$ . For  $H \geq 0.5$ , the rate of increase of  $p_{\rm p}$  slows in the range  $A_{\rm p} \sim 10^2-10^3 d_{\rm rep}^2$ . In particular, for H=0.8 there is barely any change in  $p_{\rm p}$  for the largest patches with  $A_{\rm p} \sim 10^5 d_{\rm rep}^2$ , implying that  $p_{\rm p}$  is saturating to a constant value. Data for H=0.65 and H=0.5 show a similar trend, but the lack of such large patches makes it difficult to state definitively that these curves are saturating. For H=0.3, we do not observe patches larger than  $A_{\rm p}=10^2 d_{\rm rep}^2$ , and the slope appears constant in the logarithmic regime.

Interestingly, the maximum value  $p_{\rm p}/h_0'E^*\approx 0.58$  obtained for H=0.8 is not far below Persson's value  $p_{\rm rep}/h_0'E^*\approx 0.63$ . It is conceivable based on the data shown in Fig. 4 that  $p_{\rm p}/h_0'E^*$  will saturate nearer to but likely still below this prediction in the fractal limit for H=0.8. The prediction due to Bush et al. is marked on the right-hand side of Fig. 4 and agrees most closely with the limits of the Hertz regime. The value of  $p_{\rm p}$  reached by the largest patches for each H is clearly not the same as the system-wide value  $p_{\rm rep}$ . Computed values of  $p_{\rm rep}/h_0'E^*$  shown in Figs. 1–3 are necessarily lower because of the contributions from the more numerous smaller patches. In the fractal and thermodynamic limits, the correspondence between  $p_{\rm rep}$  and  $p_{\rm p}$  is governed by the form of the patch-size distribution. We will discuss this in greater detail in the next section.

Measures such as  $p_{\rm p}$  are robust with respect to  $\zeta$  and changes in contact area. Figure 5 (a) shows that  $p_{\rm p}$  is relatively insensitive to changes in contact area for  $A_{\rm tot}/A_0 < 0.1$ . The pressure in patches smaller than  $d_{\rm rep}^2$  and in the early logarithmic regime is unaffected. The most noticeable change is the emergence of larger patches with values of  $p_{\rm p}$  that smoothly follow the continuation of curves from lower contact areas. Here, we show data only for H=0.8 for clarity but found similar behavior for smaller H.

Although  $p_{\rm p}$  does not depend on area fraction in the fractal limit, there is some dependence on  $\zeta$  for H=0.8 when  $\zeta$  is small. Figure 5 (b) demonstrates the effect of adjusting  $\zeta$  on  $p_{\rm p}$  in the range of 4-5% contact for H=0.8. The figure shows that  $p_{\rm p}$  decreases by successively smaller amounts in the logarithmic regime as  $\zeta$  grows. We conjecture that the fractal limit strongly resembles our data for  $\zeta=4096$ . The Hertz regime is unaffected because contacts with  $A_{\rm p}\lesssim d_{\rm rep}^2$  are controlled by the highest frequency wave vectors of order  $1/d_{\rm rep}$ . Curiously, the maximum  $p_{\rm p}$  remains roughly the same for all  $\zeta$ . The most pronounced effect of increasing  $\zeta$  is that the range of patch sizes extends up to two decades further as  $\zeta$  increases from 128 to 4096. We expect this trend to continue for larger  $\zeta$  for H=0.8, as will be discussed in the next section. We checked that  $p_{\rm p}$  is insensitive to  $\zeta$  for H<0.5. Given the results shown in Fig. 3, this is the case when  $\zeta>30$ .

Only patches with  $A_{\rm p} \gtrsim 10^3 d_{\rm rep}^2$  show a tendency to saturate at a plateau. The behavior of these largest patches looks essentially log-like over the full range for surfaces with  $\zeta < 1024$ . Yastrebov et al. conducted simulations in this regime and extrapolated the logarithmic scaling to conclude that  $p_{\rm rep}$  diverges in the fractal limit [50]. The results we present here demonstrate that this extrapolation is based on systems that do not generate large enough patches to probe the saturating  $p_{\rm p}$  regime, and thus misses that  $p_{\rm rep}$  remains finite.

### 3.1.3. Pressure in contacting regions: Summary and discussion

The main results of Section 3.1 concern the behavior of the mean patch pressure as determined by contact patch size. From Hertz theory, the pressure in small, compact patches rises as  $\sqrt{A_{\rm p}}$  for all H. The mean pressure in patches larger than a crossover scale of order  $d_{\rm rep}^2$  grows logarithmically before appearing to saturate at a plateau for H>0.5. The plateau value increases slightly with H but is insensitive to the long-range roughness correlation length in the fractal limit. In that limit, Persson's predicted value for the mean contact pressure gives best agreement with our numerical results for large patches; the mean contact pressure will be close to the value  $\kappa\approx0.58$  we observed in our simulations.

The large value of the mean pressure attained in large patches has important implications for elastoplastic solids. With  $h_0' \sim 0.1$ , the largest patch pressure values we computed  $p_p/E^* \approx 0.06$  are larger than the yield stress of most materials. Thus, many materials would undergo plastic flow far before the

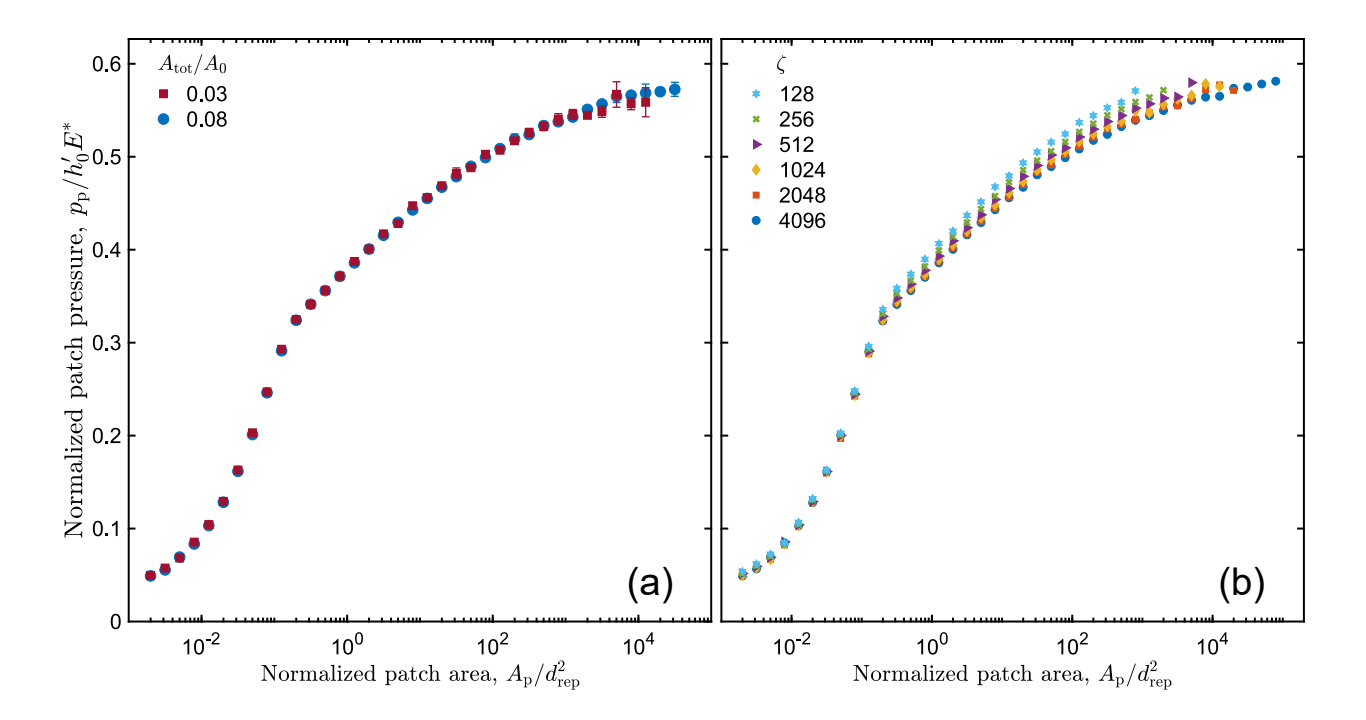


Figure 5: (a): Increasing  $A_{\rm tot}/A_0$  from 0.03 to 0.08 has negligible effects on  $p_{\rm p}/h_0'E^*$  for small  $A_{\rm p}$  but extends the curves as larger patches are introduced. Data are shown for H=0.8 but similar trends were observed for other H. (b): Shifts of the dimensionless mean patch pressure at comparable area fractions as a function of  $A_{\rm p}/d_{\rm rep}^2$  for increasing  $\zeta$ . The upwards shift apparent for intermediate  $A_{\rm p}/d_{\rm rep}^2$  as  $\zeta$  decreases is most pronounced for H=0.8 and absent for H=0.3. Note that the size of the largest patches observed also decreases with  $\zeta$ . The system size is  $32768a_0$  for  $\zeta<4096$ ; the  $\zeta=4096$  data are reproduced from Fig. 4 with  $L=65536a_0$ .

pressures we find in our simulations are reached unless the surfaces were significantly smoother at short scales, i.e.,  $h'_0 \sim 10^{-3} - 10^{-2}$ . Based on our results, the majority of plastic deformation should occur in the largest patches and the mean pressure in flowing patches should tend towards the material hardness. Interestingly, for soft solids undergoing plastic flow, the net result is that surface morphology plays less of a role overall [32].

3.2. Size of disconnected contact patches

# 3.2.1. Contact patch-size distribution

The distribution of individual (disconnected) contact patch sizes has proven challenging to pin down numerically [4, 6, 29, 32, 33, 34]. The general consensus is that the patch-size distribution has form  $n(A_{\rm p}) \sim A_{\rm p}^{-\tau}$  over at least a part of the range of patch sizes, though the exponent  $\tau$  and behavior of the tail of the distribution are less clear. Computational studies have found a variety of exponents using fits over limited data ranges, but most results agree that  $1 < \tau < 2$  for all H [4, 34]. This finding is important because all non-zeroth moments of  $n(A_{\rm p})$  are dominated by the largest contact patches for  $\tau < 2$ . For example, the total load  $F_{\rm tot}$  is given by:

$$F_{\text{tot}} = F_H + \int_{\sim d_{\text{rep}}^2}^{\infty} dA_{\text{p}} \ p_{\text{p}}(A_{\text{p}}) A_{\text{p}} \ n(A_{\text{p}}), \tag{5}$$

where  $F_H$  is the total force carried by patches smaller than the crossover scale  $\sim d_{\text{rep}}^2$ . The integral closely resembles the first moment  $\langle A_{\text{p}} \rangle$  because  $p_{\text{p}}$  grows at most logarithmically outside the Hertz branch, and like the first moment, Eq. (5) is dominated by the upper limit of the integral for  $\tau < 2$ .

Compelling recent work by Müser & Wang [34] hypothesized that  $n(A_p)$  is a power-law distribution cut off exponentially at a maximum patch size  $A_{\text{max}}$ . It is reasonable to assume that  $A_{\text{max}}$  is a function of contact area so that the power-law domain of  $n(A_p)$  broadens as contact area increases. Similar to Ref. 34, in this section we focus on H = 0.3 and H = 0.8, as these values are emblematic of the two non-marginal ranges of H (H < 0.5 and H > 0.5). We found significant changes in  $n(A_p)$  with increasing contact area and that contrary to Ref. [34], the bearing-area model exponents did not fit our data for either H=0.3(bearing-area exponent  $\tau = 1.85$ ) or H = 0.8 ( $\tau = 1.6$ ) when  $\zeta$  is large. Rather, over the regimes where the distributions could be fit by power laws, the best fit exponents were both close to 1.7. This implies that the bearing-area model understates the probability of large patches for H = 0.3 (i.e., the distribution decays less rapidly with patch size than predicted by the bearing-area model) and overstates the probability of large patches for H = 0.8 (i.e., the distribution decays more rapidly with patch size than predicted by the bearing-area model). Figure 6 (a) shows our computed  $n(A_p)$  for H=0.3 divided by the bearing-area model prediction  $n(A_p) \sim A_p^{-1.85}$ . Plotted in this way, our data reveal that the patch-size distribution obtained from elastic contact does not agree with the bearing-area model prediction over any range as the ratio generally has a positive slope outside the distribution tails and for  $A_{\rm p} \gtrsim d_{\rm rep}^2$ ; this is particularly evident for  $A_{\text{tot}}/A_0 = 0.117$ . Likewise, the distribution for H = 0.8 is shown in Fig. 6 (b) with the approximate fit power law  $A_{\rm p}^{-1.72}$  divided out (rather than the bearing-area model prediction  $n(A_{\rm p}) \sim A_{\rm p}^{-1.6}$ ). Note that for all H, the distribution of patches with size  $A_{\rm p} \lesssim d_{\rm rep}^2$  is uniform. See the Supporting Information for associated results concerning the area dependence of the bearing-area patch-size distribution for H=0.3and H = 0.8.

For H=0.3, the distribution has a narrow power-law regime that broadens with additional contact area. Figure 6 (a) shows that the distribution is cut off sharply at a maximum patch size that grows as the contact percentage increases from near 1% to about 11%. We observed that this trend continued to larger area fractions, and our estimate of  $\tau \approx 1.7$  for elastic contact stems from the distribution at roughly 30% contact (not shown). The behavior of the cutoff suggests that an analogy can be made between contact patches in elastic contact mechanics and clusters in standard percolation theory [52]. In percolation theory, the distribution of cluster sizes s has the form  $n(s) \sim s^{-\tau_{\rm pc}} e^{-s/s_{\rm max}}$ . In two dimensions (2D), the exponent for uncorrelated percolation is  $\tau_{\rm pc}=187/91\approx 2.05>2$ . The maximum cluster size  $s_{\rm max}$  diverges as a power of the inverse difference of the coverage fraction p from the percolation threshold  $p_c$ , written as  $|p-p_c|^{-1}$ . For context, recent work has estimated that elastic contact percolation occurs near 39% for H=0.3 and 42% for H=0.8 [53].

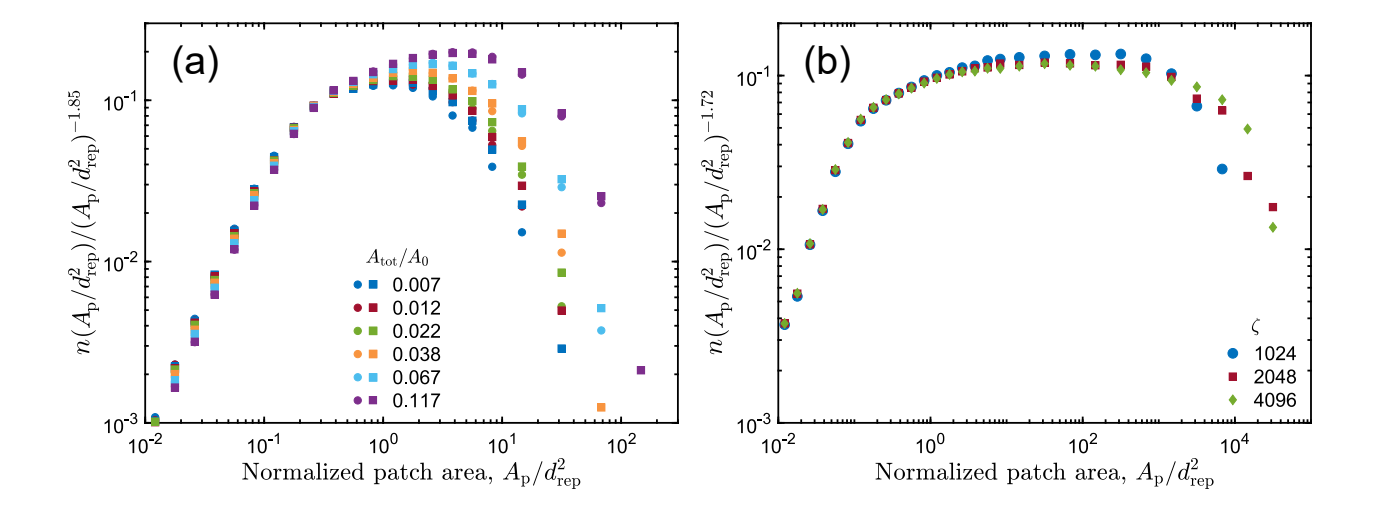


Figure 6: Contact patch-size distributions for surfaces with H=0.3 (a) and 0.8 (b). For comparison purposes, the computed distributions are divided by power-law distributions. (a): A power law with exponent  $-\tau=-1.85$  matching the bearing-area model prediction for H=0.3 is divided out to emphasize that the predicted exponent is too large to fit the data over a significant range. The system sizes are  $L=4096a_0$  (circles) and  $8192a_0$  (squares) and with  $\zeta=256$  and  $\zeta=512$ , respectively. Color indicates the values of  $A_{\rm tot}/A_0$  located in the legend. (b): A power law with exponent  $-\tau=-1.72$  is divided out for H=0.8 and fits the data over a broad scaling range. The effect of changing  $\zeta$  with fixed  $L=65536a_0$  is shown using the colors/symbols in the legend.

The notion of a diverging largest patch size is qualitatively consistent with Fig. 6 (a). In the classic percolation problem, the primary mechanism for generating larger clusters is through the unification of neighboring clusters by progressively increasing the fraction of populated sites. Percolation theory tells us that the cluster correlation length  $\xi$  grows as  $|p-p_c|^{-\nu}$ , where  $\nu$  is the correlation exponent. Working with this analogy, the contact correlation length is of order  $d_{\text{rep}}$  at low area fractions, i.e., far below percolation for H=0.3. Similarly, we conclude that the corresponding basic unit of elastic contact is a patch with area of order  $d_{\text{rep}}^2$ . Large length scales such as  $\lambda_{\text{max}}$  and L are only relevant when the correlation length has grown to be comparable in magnitude. Consequently, the patch-size distribution exhibits almost no dependence on  $\zeta$  provided that  $\zeta \gg 1$ . The system size L controls the sampling of the rapidly vanishing tail of  $n(A_p)$  and is most important in determining the size of the largest contact patches, as can be seen in Fig. 6 (a).

The analogy with percolation theory does not extend to our results for H=0.8. Figure 6 (b) shows that  $n(A_{\rm p})$  is well described by a power law over more than four decades of scaling, deviating by at most a factor of two over that range. The tail of the distribution falls more steeply than  $A_{\rm p}^{-1.72}$  and moves outwards to larger  $A_{\rm p}$  with increasing  $\zeta$ . From this we infer that  $\lambda_{\rm max}$ , not an intrinsic scale, sets the maximum patch size for H>0.5. We observed that there is a limited power-law region (not shown) that may be better fit by smaller exponents for surfaces with narrow spectral range ( $\zeta<500$ ). In these cases  $n(A_{\rm p})$  seems to be cut off in agreement with Ref. [34] for H=0.8. Despite this, our data unambiguously show that the fitting exponent converges to about 1.72 for large  $\zeta$  at low area fractions.

Our findings for  $n(A_{\rm p})$  provide insight into the variation of  $p_{\rm rep}$  with  $A_{\rm tot}/A_0$  and  $\zeta$  (or Nayak's parameter,  $\alpha$ ). From Eq. (5), the largest contact patches are most important in determining  $F_{\rm tot}$  because  $n(A_{\rm p})$  falls slower than  $A_{\rm p}^{-2}$ , while from Fig. 4 the pressure is highest in these largest patches. Increasing the contact area by applying higher loads raises the probability of the largest patches relative to small patches—by unifying patches for H=0.3 or by growing existing patches for H=0.8. Both pathways result in new maximum-size patches that become still more important as the contact area grows. Consequently,  $p_{\rm rep}$  increases with  $A_{\rm tot}/A_0$  (see Fig. 1) to reflect the high pressure contributions of the more heavily weighted large size patches.

The patch-size distribution also sheds light on the dependence of  $p_{\rm rep}$  on  $\zeta$  we demonstrated earlier in

Fig. 3 for different H. Fig. 3 shows that for H=0.3, provided that  $\zeta>100$  there is essentially no dependence on its value, a result in keeping with our observations that changing  $\zeta$  had no impact on  $n(A_{\rm p})$  or  $p_{\rm p}$ . On the other hand, for H=0.8 the size of the largest patch increases with  $\zeta$ . Note also that we showed in Fig. 5 (b) that  $p_{\rm p}$  also depends on  $\zeta$  for  $\zeta<4096$ . Thus,  $p_{\rm rep}$  continues to rise with  $\zeta$  for small systems (as measured by  $\zeta$ ), while in the fractal limit, the mean contact pressure will simply attain the value of  $p_{\rm p}$  in the largest patch.

#### 3.2.2. Characteristic and maximum patch sizes

To illustrate the effect of contact area on the evolution of the elastic contact patch-size distribution, we define the characteristic patch size  $A_c$  using the contra-harmonic mean [34]:

$$A_{\rm c} = \frac{\langle A_{\rm p}^2 \rangle}{\langle A_{\rm p} \rangle} = \frac{\int dA_{\rm p} \ n(A_{\rm p}) A_{\rm p}^2}{\int dA_{\rm p} \ n(A_{\rm p}) A_{\rm p}}.\tag{6}$$

The contra-harmonic mean measures the mean size of a patch to which a randomly chosen contact node belongs. Assuming  $n(A_{\rm p}) \sim A_{\rm p}^{-\tau}$  with  $1 < \tau < 2$  between patch sizes of order  $d_{\rm rep}^2$  up to a hypothetical maximum patch size  $A_{\rm max} \gg d_{\rm rep}^2$ , Eq. (6) evaluates to  $A_{\rm c} \approx \frac{2-\tau}{3-\tau}A_{\rm max}$ . Our numerical results for  $A_{\rm c}/d_{\rm rep}^2$  are plotted in Fig. 7 for three different H at fixed  $L=16384a_0$  and varying  $\zeta$ .

Figure 7 (a) shows that  $A_c$  rises from values of order  $d_{\text{rep}}^2$  before beginning to diverge near 10–20% contact as the onset of percolation becomes apparent for all H. Note that the non-zeroth moments (including  $A_c$ ) of  $n(A_p)$  all diverge (with different exponents) at the percolation threshold. For H=0.3,  $A_c$  gradually increases at low area fractions and there is little dependence on  $\zeta$ , consistent with our observation that  $n(A_p)$  is also insensitive to  $\zeta$  for H<0.5. For H=0.8,  $A_c$  grows as a power of  $A_{\text{tot}}/A_0$  from initial contact and is independent of  $\zeta$  below  $10^{-4}$  area fraction. At increasingly large area fractions as  $\zeta$  increases (e.g., compare  $\zeta=1024$  with  $\zeta=128$ ),  $A_c$  falls below the low area fraction power-law trend. Correspondingly, there is a nearly proportional increase in  $A_c/d_{\text{rep}}^2$  with each doubling of  $\zeta$  at fixed area fraction, as shown most clearly for  $A_{\text{tot}}/A_0 > 10^{-2}$ . We include data for H=0.5 in Fig. 7 (a) as an intermediate case; the data resemble H=0.3 but there is slight spread that is roughly logarithmic. As a final aside pertinent to these results, at initial contact we observed that fixed-load simulations exhibited less variability in values of  $A_c$  as compared to fixed-displacement protocols, notably for H=0.8.

Figure 7 (b) focuses on data for H=0.3 and illustrates that  $A_{\rm c}$  shows at most logarithmic growth for large L as  $A_{\rm tot}/A_0$  increases from  $O(10^{-5})$  to  $O(10^{-2})$ . The data collapse without scaling factors for large  $L/\lambda_{\rm min}$ , with the onset of the collapse moving to smaller area fractions with increasing  $L/\lambda_{\rm min}$ . The smallest systems we studied never joined the master curve but are included to show the limits of the collapse. Referring to Fig. 6 (a), the values of  $A_{\rm c}/d_{\rm rep}^2$  below 10% contact lie just within the tail of  $n(A_{\rm p})$  where sampling of large patches is controlled by L.

Conversely, Fig. 7 (c) reveals that  $A_{\rm c}$  strongly depends on  $\zeta$  for H=0.8. As we noted earlier,  $A_{\rm c}$  is closely linked to the size of the largest patch when the power-law range of the distribution is broad; in addition, the distribution tail moves outwards with increasing  $\zeta$ . Scaling  $A_{\rm c}/d_{\rm rep}^2$  by  $\zeta^{1.55}$  collapses the data above roughly 5% contact and accomplishes a decent collapse at lower area fractions for each fixed value of  $L/\lambda_{\rm max}$  (as indicated in the figure by the use of different symbols). The factor  $\zeta^{1.55}$  is consistent with a similar finding by Ref. [34]. The results in Fig. 7 (c) show that the characteristic patch size depends only on  $\zeta$  where all the data collapse, but for lower area fractions  $A_{\rm c}/d_{\rm rep}^2$  depends only on L; for example, compare with the H=0.8 results for  $A_{\rm tot}/A_0 < 10^{-3}$  in Fig. 7 (a), which were computed using fixed L and varying  $\zeta$ . The spread evident in Fig. 7 (c) at initial contact and area fractions up to the collapse is caused by the  $\zeta$  rescaling, which instead groups data by  $L/\lambda_{\rm max}$ , as indicated by the use of symbols for constant  $L/\lambda_{\rm max}$ .

It is important to understand how the size of the mean largest patch  $\langle A_{\rm max} \rangle$  evolves with area fraction, as well as its dependence on  $\zeta$  and L. Plainly, the largest patch found for H=0.3 is governed by the cutoff of  $n(A_{\rm p})$ , while Fig. 6 (b) and Fig. 7 (c) jointly suggest that  $\zeta$  is most important in determining  $\langle A_{\rm max} \rangle$  for H=0.8. Our results for  $\langle A_{\rm max} \rangle$  are shown in Fig. 8. The approach to the fractal limit is evident for H=0.3 in Fig. 8 (a), similar to what we found for  $A_{\rm c}$  in Fig. 7 (b). However,  $\langle A_{\rm max} \rangle$  scales as  $(L/\lambda_{\rm min})^{0.4}$  and also grows slowly with contact area below 10% contact. This finding is unsurprising because pushing solids

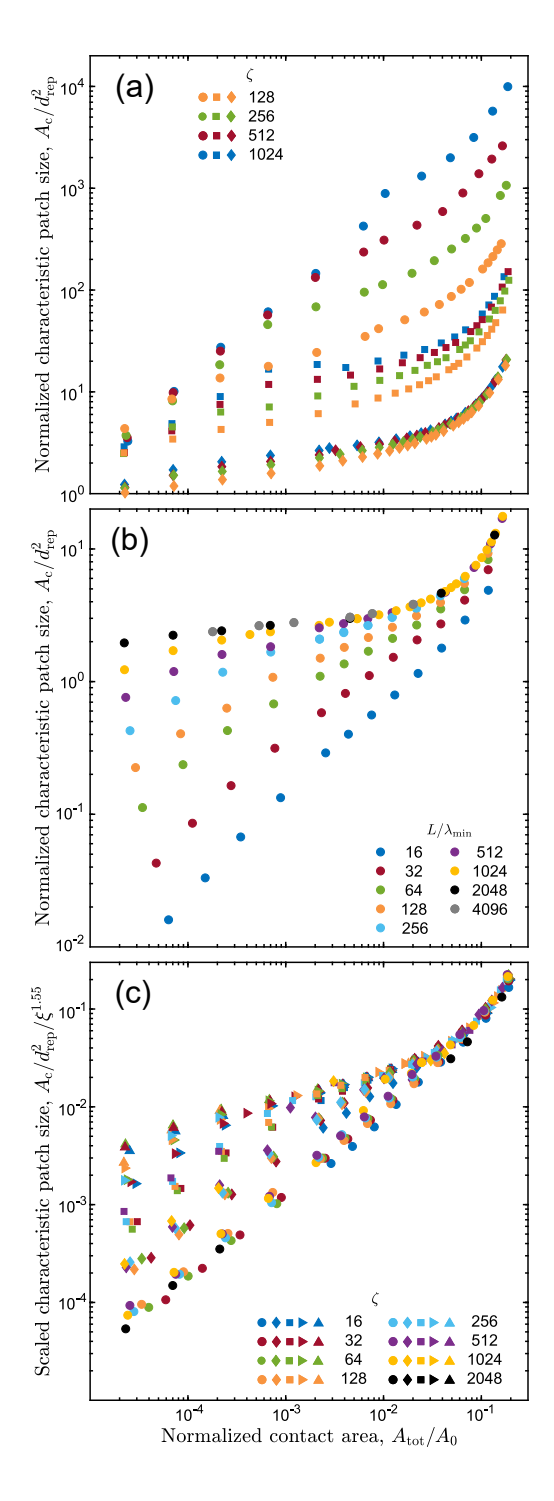


Figure 7: (a): Characteristic patch size as a function of total contact area for the indicated H (H=0.3 as diamonds; H=0.5 as squares; H=0.8 as circles) and  $\zeta$  (colors). The system side length is  $16384a_0$ . (b): System size dependence of the characteristic patch size for H=0.3. Here,  $L=\lambda_{\rm max}$  and is varied by factors of 2 ( $\lambda_{\rm min}$  fixed; see Methods) as indicated in the legend. (c): Characteristic patch size for H=0.8 normalized by  $\zeta^{1.55}$  to collapse the data above roughly 5% contact. Color indicates  $\zeta$  while symbols signify values of  $L/\lambda_{\rm max}$ : 1 (circles), 2 (diamonds), 4 (squares), 8 (rightwards triangles) and 16 (upwards triangles).

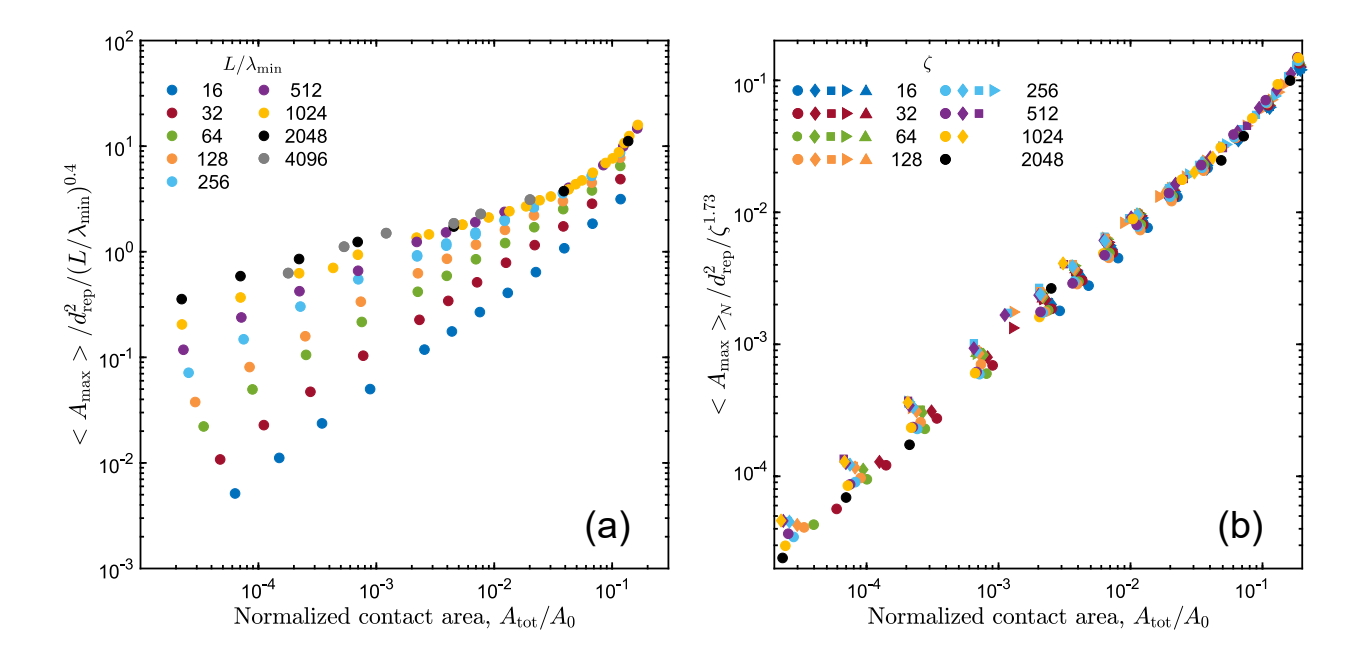


Figure 8: (a): The scaled size of the (ensemble-averaged) single largest patch for H=0.3 and the values of  $L/\lambda_{\rm min}$  indicated in the legend. The scaling factor  $(L/\lambda_{\rm min})^{0.4}$  is chosen to collapse the data above 1% contact for large  $L/\lambda_{\rm min}$ . (b): The scaled mean area contained within the largest  $N=(L/\lambda_{\rm max})^2$  patches for H=0.8. The scaling factor  $\zeta^{1.73}$  is chosen to best collapse the data above 3% contact, though an approximate collapse is achieved over the full range of contact patch sizes. Color indicates  $\zeta$  while symbols signify values of  $L/\lambda_{\rm max}$ : 1 (circles), 2 (diamonds), 4 (squares), 8 (rightwards triangles) and 16 (upwards triangles).

further into contact can cause existing patches to expand and/or to merge with other patches. We conjecture that the dependence of  $\langle A_{\rm max} \rangle$  on L for H=0.3 stems from improving sampling of the distribution tail with increasing system size, as supported by Fig. 6 (a). Again,  $\zeta$  is irrelevant at low area fractions where the contact correlation length is comparable to  $d_{\rm rep}$ .

We observed earlier in Fig. 6 (b) that  $\zeta$  controlled the tail of the distribution for H=0.8. When the correlation length is comparable to  $\lambda_{\rm max}$  (as is the case for H=0.8), the contact interface can be regarded as being composed of  $N=(L/\lambda_{\rm max})^2$  statistically-independent regions each containing a patch with size of order  $\langle A_{\rm max} \rangle$ . Of course, there is always a globally maximum patch, but its size is controlled by fluctuations about the ensemble average. To account for this, we compute the mean largest patch size  $\langle A_{\rm max} \rangle_N$  obtained by averaging over the sizes of the N largest patches. Figure 8 (b) shows that  $\langle A_{\rm max} \rangle_N$  collapses up to a factor of two when normalized by  $\zeta^{1.73}$  over nearly four decades, irrespective of L. These results indicate that the size of the average largest patch grows with both the total fractional contact area and non-trivially with  $\zeta$  as  $\zeta^{1.73}$ . The latter result affirms that increasing  $\lambda_{\rm max}$  permits the formation of larger and larger contact patches, as we saw earlier in Fig. 6 (b). It is interesting to note that this scaling is valid even down to  $\zeta < 100$ . The discrepancy between the exponent 1.55 used in Fig. 7 (c) and the exponent 1.73 used here may be due to a log-like correction in the relationship between  $A_{\rm c}$  and  $\langle A_{\rm max} \rangle_N$ , which can easily account for a change in exponent of approximately 0.2. Curiously, the scaling exponent 1.73 is nearly identical to the estimated H=0.8 patch-size distribution exponent  $\tau=1.72$ ; however, we know of no obvious explanation for the near equivalence of the two exponents.

# 3.2.3. Size of disconnected contact patches: Summary and discussion

The main results of Section 3.2 concern the dependence of the patch-size distribution and its moments on the roughness structure. We showed that the behavior of the patch-size distribution as the total contact area grows is qualitatively different above and below H = 0.5. For H < 0.5, the distribution is cut off by a maximum patch size which diverges with increasing contact area in a manner consistent with percolation

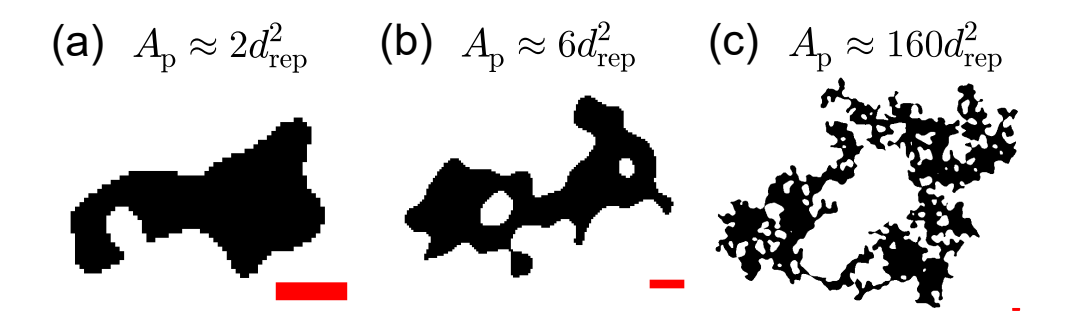


Figure 9: Example contact patches of varying size for H=0.8. The red scale bar indicates  $\lambda_{\min}=16a_0\approx 2/3d_{\mathrm{rep}}$ . (a): A typical contact patch with  $A_{\mathrm{p}}\approx 2d_{\mathrm{rep}}^2$ . Contact patches this size are usually compact. (b): A typical contact patch with  $A_{\mathrm{p}}\approx 6d_{\mathrm{rep}}^2$ . Contact patches this size usually contain one or two bubbles. (c): A typical contact patch with  $A_{\mathrm{p}}\approx 160d_{\mathrm{rep}}^2$ . Contact patches this size always have many bubbles and usually only occur for H>0.5 at low area fractions.

theory. At low area fractions, the maximum patch size is usually much smaller than  $\lambda_{\rm max}$ , rendering long-range roughness correlations irrelevant. The system size, on the other hand, controls sampling of the distribution tail. The patch-size distribution for H>0.5 is a power law over 3–4 decades of  $A_{\rm p}$  and is limited by  $\zeta$  rather than a constant, intrinsic maximum patch size. For H=0.8, we find that the patch-size distribution depends only weakly on area fraction in the 1–10% contact regime.

As the patch-size distribution decays slower than  $A_{\rm p}^{-2}$ , regardless of H, most contact quantities are dominated by the largest patches. Considering the area-weighted sum used to calculate the applied load (Eq. 5), our simulations show that  $p_{\rm rep}$  will be arbitrarily close to the pressure expected for the largest patches observed at a given fractional contact area. Consequently, the value of  $p_{\rm rep}$  changes slowly but is typically within 10% of  $0.5h_0'E^*$  in the low area fraction regime if  $\zeta$  is large.

### 3.3. Geometry of disconnected contact patches

### 3.3.1. Contact patch classification and "bubbles"

We have already seen that  $p_{\rm p}$  differs substantially between small patches and those containing area many times larger than  $d_{\rm rep}^2$ . In this section we will show that the contact patch geometry undergoes a similar crossover with increasing patch size. The smallest contact patches ( $A_{\rm p} \lesssim d_{\rm rep}^2$ ) are formed by peak-to-peak contact; these patches are generally compact with simple circle-like shapes. Earlier, we showed that Hertz theory accurately predicts the mean pressure as a function of patch size under the assumption that  $R_{\rm asp}$  describes the typical asperity radius.

Contact patches with  $A_{\rm p} \gtrsim d_{\rm rep}^2$  are formed when ridges connecting the peaks of asperities are pushed into contact. These patches are often branched as depicted in Fig. 9 (a). From Fig. 4, the mean pressure in these patches grows logarithmically with size. We find that most patches with area exceeding around  $3d_{\rm rep}^2$  contain non-contacting regions that we dub "bubbles", as shown in Fig. 9 (b). Bubbles are formed by connecting contacts along ridges between peaks, leaving the valleys between out of contact. A simple explanation for this outcome is that the elastic energy cost of deformation is largest for the shortest scales, meaning that valleys are the last regions to be pushed into conformal contact.

Figure 9 (c) depicts a large contact patch ( $A_{\rm p}\approx 160d_{\rm rep}^2$ ) with small-scale details still visible. Patches this size always have many bubbles giving them a Swiss-cheese-like structure. For H=0.8, there is a relatively broad distribution of bubble sizes because large patches can encompass both shallow and deep valleys. As shown in Fig. 4, the pressure in these patches begins to saturate for H>0.5.

Figure 10 demonstrates that the distribution of bubble sizes  $A_{\rm b}$  decays at least as quickly as  $A_{\rm b}^{-2}$  over the entire range for all H. Consequently, the mean bubble size  $\langle A_{\rm b} \rangle$  is dominated by small sizes and remains close to  $d_{\rm rep}^2$ . Note that over limited ranges the distributions for H > 0.5 have exponents close to -2, reflecting the relatively high probability for bubbles with sizes  $10d_{\rm rep}^2$  or larger. Figure 9 (c) provides visual

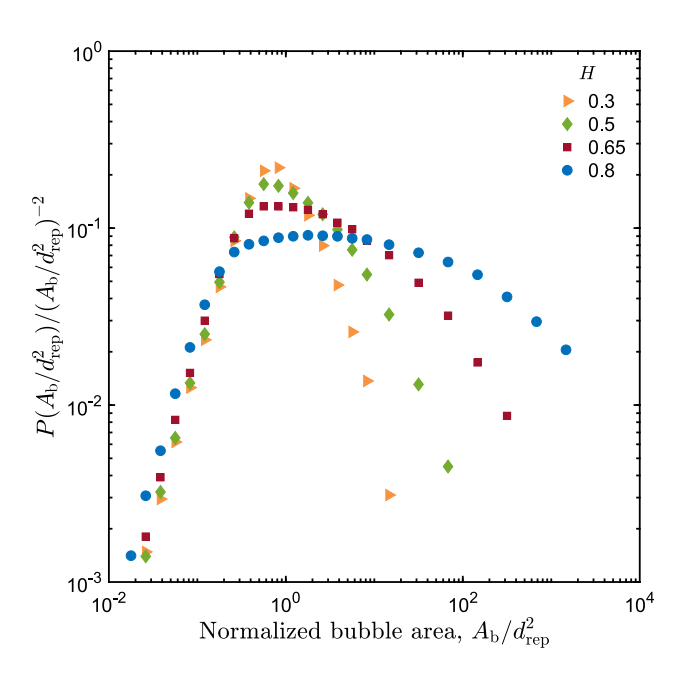


Figure 10: The distribution of bubble sizes with the power law  $A_{\rm b}^{-2}$  divided out for the indicated H. For H=0.3 and H=0.5,  $L=32768a_0$  and  $\zeta=2048$ . For H=0.65 and H=0.8,  $L=65536a_0$  and  $\zeta=4096$ .

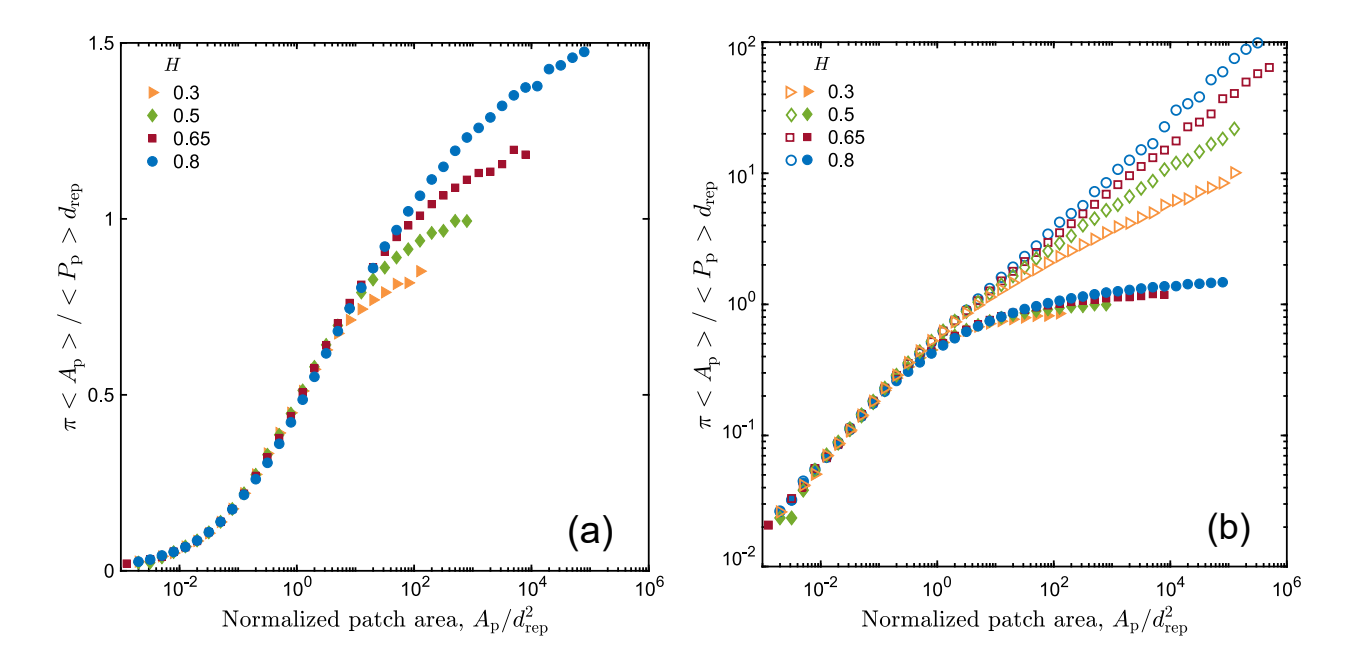


Figure 11: (a): The ratio of the mean cross-sectional diameter of contact patches to the predicted value  $d_{\rm rep}$  as a function of patch area for the indicated H. For H=0.3 and H=0.5,  $L=32768a_0$  and  $\zeta=2048$ . For H=0.65 and H=0.8,  $L=65536a_0$  and  $\zeta=4096$ . (b): A log-log representation of the same data with the addition of results for the bearing-area model at similar area fractions. Solid symbols correspond to results from the full elastic calculation, while open symbols show results for the bearing-area model.

support for this result.

### 3.3.2. Diameter of contact patches

Pastewka and Robbins [2] showed that the measured global mean contact diameter is given by the ratio  $\pi A_{\rm tot}/P_{\rm tot}$  for isotropic roughness provided  $\pi A_{\rm tot}/P_{\rm tot}\gtrsim 10a_0$ , consistent with the limits stipulated by Yastrebov et al. [49]. Here, our aim is to determine the relationship between individual contact patch diameters and areas, with the former defined as  $d_{\rm p}=\pi A_{\rm p}/P_{\rm p}$ . Figure 11 (a) summarizes our findings expressed as the ratio  $d_{\rm p}/d_{\rm rep}$ . Similar to the mean patch pressure, the mean contact diameter collapses for all H in the small patch regime when plotted as  $A_{\rm p}/d_{\rm rep}^2$ . The typical diameter of simple geometrical shapes grows as  $d_{\rm p} \propto \sqrt{A_{\rm p}}$  and the data for patches with  $A_{\rm p} \lesssim d_{\rm rep}^2$  follow this scaling. Just as for  $p_{\rm p}$ ,  $\lambda_{\rm min}$  controls the contact resolution and hence the power-law scaling of  $d_{\rm p}$  down to the smallest patches.

Again analogous to the behavior of the mean patch pressure, the growth of the contact diameter of patches of intermediate size  $(A_{\rm p} \gtrsim 3d_{\rm rep}^2)$  slows dramatically. The ratio  $d_{\rm p}/d_{\rm rep}$  in the largest patches is closest to unity for H=0.5, while  $d_{\rm rep}$  under-predicts the mean diameter for H>0.5 and over-predicts the diameter for H<0.5. The slow increase in contact diameter with patch area can be understood by considering the impact of bubbles on the geometry of large patches. Compact (bubble-free) patches can only grow by expanding their outer perimeter, whereas patches with bubbles can expand at both interior and exterior contact edges. By tracking the behavior of individual patches, we observed that expanding patches tend to enclose new bubbles even as existing bubbles shrink so that the overall change of  $d_{\rm p}/d_{\rm rep}$  was quite small. The high mean patch pressures in large patches we measured numerically may lead to partial filling-in of bubbles (accounting for the slow increase of  $d_{\rm p}$  in Fig. 11 (a)), but are evidently too small to achieve conformal contact on the scale of  $d_{\rm rep}$  [54, 55]. The saturating values of  $d_{\rm p}/d_{\rm rep}$  shown in Fig. 11 (a) imply equal growth rates for patch contact area and perimeter due to the combination of these effects, and provide evidence for the fractal nature of the largest patches.

In Fig. 11 (b), we directly compare contact diameter results for elastic contact with the bearing-area model. In the bearing-area model, the contact diameters of patches larger than approximately  $3d_{\rm rep}^2$  exhibit power-law scaling with  $A_{\rm p}$ . The figure shows that the associated exponents depend upon H, as we will address in subsequent paragraphs. The results from panel (a) are re-plotted in panel (b); the log-log axes representation crystallizes the striking near-saturation of the contact diameter in large patches in elastic contact, where  $d_{\rm p}/d_{\rm rep}$  grows by at most a factor of 3/2 for patches with  $A_{\rm p} > d_{\rm rep}^2$ .

3.3.3. Fractal dimension of contact patch area and perimeter

Contact patches formed between self-affine surfaces are commonly supposed to be fractal. We define distinct fractal dimensions for the contact patch perimeter and contact patch area that satisfy  $P_{\rm p} \sim R^{D_{\rm p}}$  and  $A_{\rm p} \sim R^{D_{\rm A}}$ , where R is the radius of the smallest disk that contains the entire patch. To distinguish separate pairs of fractal exponents for specific contact models, we append additional subscripts in the text as shorthand; e.g. for elastic contact we use  $D_{\rm A,E}$  and  $D_{\rm P,E}$ . Fractal exponents without additional subscripts refer to the collective case. We also identify the fractal dimension  $D_{\rm P,C}$  of the exterior (non-bubble) patch perimeter, which we denote  $P_{\rm ext}$ , and for the fractal dimension  $D_{\rm A,C}$  of the total area  $A_{\rm fill}$  (i.e., the compact area, or contact area + bubble area) enclosed by the exterior boundary. To isolate the exterior patch perimeter and compact patch area, we fill in all bubbles to enforce compactness. After performing this procedure, the only contribution to the compact patch perimeter is the outermost interface and the entire interior is considered to be in contact.

With the scaling relations above, the mean contact diameter can be expressed in terms of the difference between the fractal dimensions of patch areas and patch perimeters, namely:

$$d_{\rm p} \propto \frac{A_{\rm p}}{P_{\rm p}} \sim R^{D_{\rm A} - D_{\rm P}}.\tag{7}$$

Similar relationships can be written for compact patches and for the bearing-area model. The elastic contact results in Fig. 11 (b) imply that  $D_{\rm A} \geq D_{\rm P}$  for patches bigger than  $d_{\rm rep}^2$ , where the equality holds if  $d_{\rm p}$  truly saturates in the fractal limit. Figure 11 (b) further hints that the fractal dimensions for patch perimeter and area from the bearing-area model are different and that the difference grows with H. Patches produced by the bearing-area model are assumed to be 2D with fractal boundaries [38, 56]. Kondev and Henley [37]

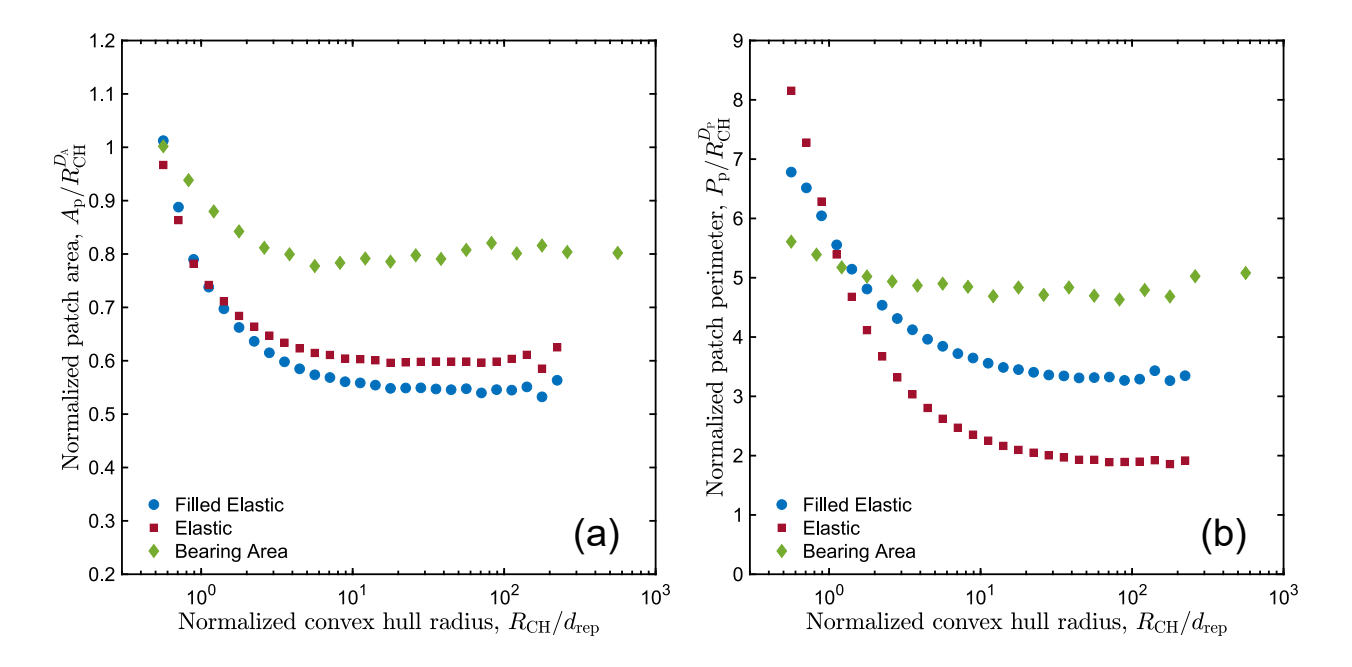


Figure 12: (a): Patch areas normalized by a power law  $R_{\rm CH}^{D_{\rm A}}$  to estimate fractal dimensions for large patches obtained from elastic calculations and from the bearing-area model for H=0.8. The fractal exponents  $D_{\rm A,\_}$  are 1.89 for elastic contact (squares), 1.97 for filled-in patches from elastic contact (circles) and 1.98 for the bearing-area model (diamonds). The side length is  $65536a_0$  and  $\zeta=4096$ . (b): The same procedure was repeated to obtain estimates for the fractal dimensions of patch perimeters for H=0.8. The fractal exponents  $D_{\rm P,\_}$  are 1.83 for elastic contact (squares), 1.51 for filled-in patches from elastic contact (circles) and 1.18 for the bearing-area model (diamonds).

argued that the fractal dimension of the perimeter of such patches is  $D_{\rm P,BA} = (3-H)/2$ , yielding the scaling relation  $A_{\rm p}/P_{\rm p} \sim A_{\rm p}^{(1+H)/4}$ . When H=1 this scaling relation reduces to the trivial result,  $d_{\rm p} \sim \sqrt{A_{\rm p}}$ , found for simple shapes. We checked the validity of the predicted scaling for our bearing-area results in Fig. 11 (b) and found that it is approximately correct, but for best agreement the small population of bubbles generated in the bearing area needed to be filled in using the procedure outlined earlier. Forcing all patches to be compact effectively ensures that they are 2D with respect to patch area.

Calculating the fractal dimension of contact patches by determining the minimum enclosing disk is computationally intensive, so instead we determined the area of the convex hull  $A_{\rm CH}$  and exploited the relationship  $R \sim R_{\rm CH} \equiv \sqrt{A_{\rm CH}}$ . We focus on data for H=0.8 in order to have at least one decade of scaling over which to estimate the fractal dimensions of large patches. In the trivial case of small patches, the area and perimeter fractal dimensions are equal to the topological dimensions, i.e.  $D_{\rm A}=2$  and  $D_{\rm P}=1$ . Our results comparing fractal dimensions for area and perimeter for the bearing-area model and elastic contact with and without filling in bubbles are shown in Fig. 12. To highlight discrepancies in scaling, we have divided out power laws with the estimated fractal dimension exponents.

For surfaces with H=0.8 in elastic contact, we estimate that the patch area fractal dimension is  $D_{\rm A,E}=1.89\pm0.03$  and  $D_{\rm P,E}=1.83\pm0.04$  for the patch perimeters. This result is consistent with our observation that  $d_{\rm p}$  grows slowly with patch size in elastic contact. Indeed, logarithmic growth and power-law growth with exponents smaller than 0.1 are essentially indistinguishable over just two decades of scaling. The corresponding compact elastic contact patches have  $D_{\rm A,C}=1.97\pm0.03$  and  $D_{\rm P,C}=1.51\pm0.03$  for patch area and external perimeter, respectively. It is interesting that bubbles have only a small effect on the fractal dimension of the patch area, reducing the exponent from 1.96 to 1.89. On the other hand, bubbles have a markedly strong effect on the fractal dimension of the perimeter, which jumps from 1.51 to 1.83 when bubbles are included in the calculation. These observations signify that bubbles are the main driver for the saturation of the mean contact diameter in large patches because they significantly increase the patch

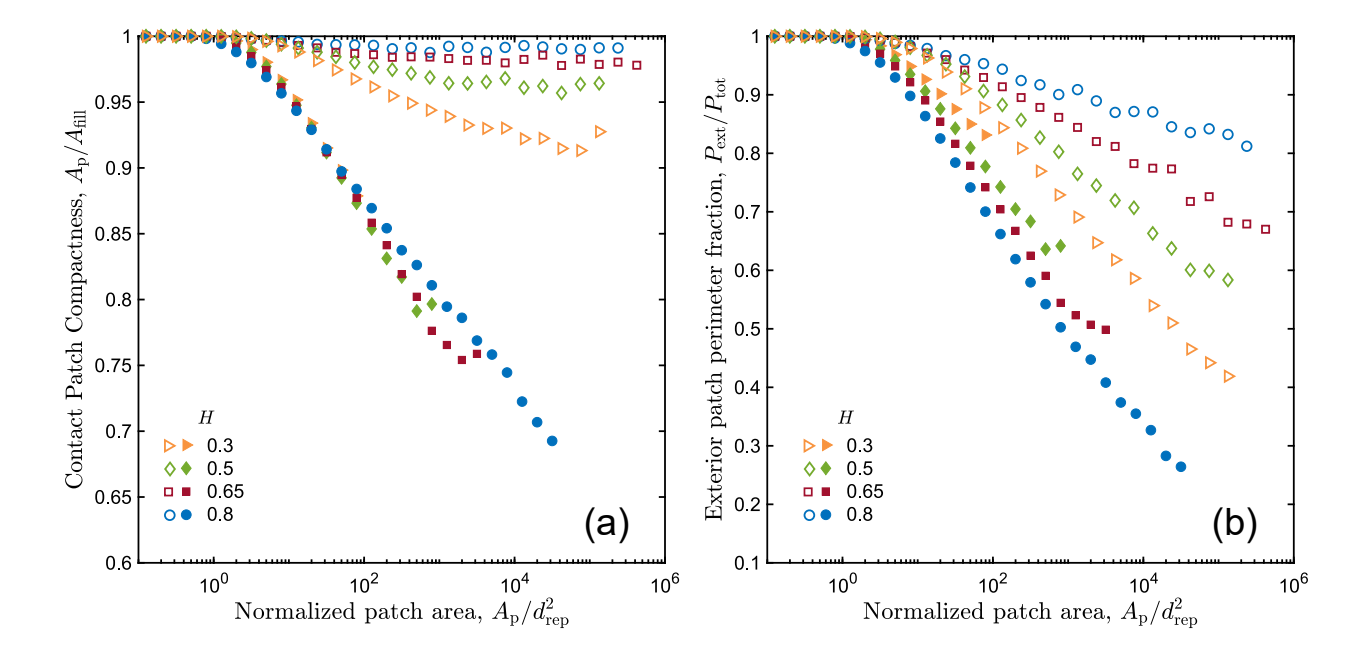


Figure 13: (a): The ratio  $A_{\rm p}/A_{\rm fill}$  as a function of  $A_{\rm p}/d_{\rm rep}^2$  for the indicated H. Elastic contact results are shown with filled symbols and open symbols correspond to results for the bearing-area model at similar area fractions. For H=0.3 and H=0.5,  $L=32768a_0$  and  $\zeta=2048$ . For H=0.65 and H=0.8,  $L=65536a_0$  and  $L=65536a_0$ 

perimeter while only slightly reducing the total contact area.

The bearing-area model produces contact patches with  $D_{\rm A,BA}=1.98\pm0.02$  and  $D_{\rm P,BA}=1.18\pm0.03$ . Unsurprisingly, our results show that both compact-elastic and bearing-area patch areas are essentially 2D objects. The predicted exponent for the bearing-area patch perimeter for H=0.8 is  $D_{\rm P,BA}=(3-H)/2=1.1$ . The overall contribution of bubbles to patch perimeter and area is minimal for H=0.8 in the bearing-area model, but repeating the filling-in procedure here slightly improved agreement between our result and the predicted value by reducing our estimate to  $1.15\pm0.03$ .

### 3.3.4. Contact patch compactness

To demonstrate the prevalence of bubbles in intermediate- and large-size contact patches, we compute the ratio of the true patch contact area to the filled-in patch contact area as a measure of patch compactness for elastic and bearing-area contact. Figure 13 (a) shows that in either case patches smaller than  $d_{\rm rep}^2$  are always compact, but the compactness of patches larger than  $d_{\rm rep}^2$  decreases in a logarithmic manner. In elastic contact, the slope of the drop is insensitive to H and does not saturate within the range of patch sizes accessible to our simulations. Compactness is also unaffected by contact area (at low contact area values) provided that the patch-size distribution is well sampled. Extrapolating the elastic contact data for H=0.8 suggests that patches larger than roughly  $10^6 d_{\rm rep}^2$  will contain a larger fraction of bubble area than contact area.

Our results for the bearing-area model confirm that this model produces nearly compact contact patches. Compactness is lowest for H=0.3 and approaches unity with increasing H. This stems from the anti-correlated roughness for H<0.5, as the surface slope switches sign over scales larger than  $\lambda_{\min}$ . At a given low contact area fraction, cross-sectional cuts are likely to encompass the shallow valleys common to H<0.5 surfaces, resulting in bubbles. The converse is true for H>0.5, where the surface slope persists over longer distances leading to larger amplitude roughness.

In the same spirit as patch compactness, the fractional contribution of the exterior perimeter to the total patch perimeter is simple to compute. Our results for this quantity are shown in Fig. 13 (b). As above, the ratio is unity for patches smaller than about  $d_{\text{rep}}^2$  which only have external contact edges. The elastic

contact perimeter ratio also drops in a log-like manner, in this case with slope that decreases slightly with H for patches larger than  $d_{\text{rep}}^2$ . The slope is slightly steeper than we found for patch compactness. The external perimeter outweighs the contributions from bubbles until patches are about  $10^3 d_{\text{rep}}^2$  for H = 0.8, and the ratio shrinks to about 1/4 in the largest patches we observed. Our discussion of fractal dimensions suggested that the effect of bubbles is more pronounced for the perimeter, and that is borne out here for H = 0.8 as over the same range of  $A_p/d_{\text{rep}}^2$  the compactness drops 30% but the external perimeter ratio falls 75%.

We also plot the perimeter ratio for the bearing-area model in Fig. 13 (b). Interestingly, the change in logarithmic slope with H is reversed for bearing-area results. Our results are most similar for H = 0.3, once again because the surface slope anti-correlation favors the formation of bubbles via planar cuts, while for H > 0.5 most of the interior perimeter contributions from bubbles are lost in the bearing-area model. Note also that the bearing-area model tends to produce much larger contact patches than does elastic contact at the same area fraction.

3.3.5. Geometry of disconnected contact patches: Summary and discussion

The main results of Section 3.3 concern the changes in patch geometry with patch size. Small patches with  $A_{\rm p} < d_{\rm rep}^2$  formed by the tops of touching asperities are generally compact. The mean diameter of such patches rises as  $\sqrt{A_{\rm p}}$  as expected for simple geometric shapes. Patches with  $A_{\rm p} > d_{\rm rep}^2$  are typically branching and irregular with bubbles of non-contact enclosed within the interior. The largest of these patches always include many bubbles and resemble Swiss cheese. Bubbles are a consequence of the high elastic energy cost required to deform material at the smallest scales. The primary impact of the bubbles is on the mean contact diameter, which saturates for patches with  $A_{\rm p} \gg d_{\rm rep}^2$ ; constant contact diameter occurs when the fractal dimensions for contact area and perimeter are equal. The effect is absent for the bearing-area model for which the patch diameter grows as a power of the patch area. We verified the expected scaling of the patch diameter in the bearing-area model using relationships from earlier analytic work.

We provided estimates of  $D_{\rm A}$  and  $D_{\rm P}$  for large patches from both elastic calculations and the bearingarea model for H=0.8. Elastic contact patches have fractal areas and perimeters owing to the presence of bubbles, and the fractal dimensions we estimated for patch area and patch perimeter differed by less than 0.1. The similarity of their fractal dimensions explains the approximate proportionality between contact area and perimeter implied by constant  $d_{\rm p}$ . We found that contact patches in the bearing-area model are nearly 2D and have fractal perimeters with dimensions close to predicted values. As such, the bearing-area model provides a fundamentally incompatible picture of the morphology of elastic contact and almost always overestimates the total contact area.

For elastic contact, filling in bubbles revealed that the total patch perimeter is dominated by contributions from interior bubbles in patches larger than  $\sim 10^3 d_{\rm rep}^2$ , while the effect of bubbles on contact area is relatively small. The net result is that the patch area fill fraction ratio, or compactness, drops by less than a third in the largest patches while the majority of the total perimeter of the same patches comes from bubbles. Thus, interfacial-structure-dominated quantities that depend on the total contact area such as thermal and electrical conductivity will be less sensitive to surface structure than adhesion, which also depends on the total contact perimeter.

The relationship between repulsive contact area and contact perimeter has important ramifications for the study of adhesive contact in the Derjaguin-Muller-Toporov (DMT) limit [57]. In this limit, weak but long-range adhesive forces reduce the overall load required to produce a given contact area, but leave the contact topography unchanged. Appreciable adhesive forces originate only from narrow bands of surface encircling load-bearing regions. Pastewka and Robbins developed a stickiness criterion for rough surfaces by relating the repulsive area to the area contributing substantially to adhesion. Their theory assumed that the contact perimeter is proportional to the contact area [2, 29]. Using similar assumptions about the geometry of contact patches and near-contact regions, Monti et al. used analytic results supported by numerical simulations to show that the distribution of interfacial separations or gaps g diverges as  $g^{-1/3}$  with a prefactor proportional to the contact area fraction in the DMT limit [3]. The results of both studies hinged on the mean contact diameter attaining a finite value, meaning that the contact area and perimeter

are proportional. The results we have presented in Section 3.3 support this assumption in the main because the contact diameter rises at most as  $\log A_{\rm p}$  in the largest patches, which contribute the most to the total contact area and perimeter. Moreover, for H>0.5 we conclude that contributions from small patches that violate the linear patch area-perimeter relationship are largely irrelevant in the fractal limit because the distribution of patch sizes is an untruncated power-law with (negative) exponent  $\tau<2$ .

#### 4. Conclusion

We performed large-scale nonadhesive contact simulations with billions of degrees of freedom for elastic solids with self-affine fractal surfaces to determine how the properties of contact patches depend on patch size and correlations in the roughness. We showed that subtle changes in the mean contact pressure with Hurst exponent and the roughness correlation lengths can be attributed to sampling of universal curves describing the systematic variation of the mean patch pressure with patch size. We also showed that large contact patches contain out of contact regions which have important ramifications for patch geometry and fractal behavior. Lastly, the simulations we conducted represent a significant step towards providing a precise description of the patch-size distributions for different Hurst exponents in the fractal limit, which have been challenging to formulate to date.

#### Acknowledgments

We thank Martin H. Müser and Antoine Sanner for useful discussions. We also thank Antoine Sanner for MPI-parallelization of the contact mechanics code. We used the CONTACT.ENGINEERING ecosystem (https://github.com/ContactEngineering/) for all calculations. This work is based on material funded by the US National Science Foundation (Grant Nos. DMR-1411144 and DMR-1929467) and the Deutsche Forschungsgemeinschaft (grants PA 2023/2 and EXC-2193/1 – 390951807). We also thank the DAAD for funding a short stay of JMM to Freiburg. Simulations were carried out on NEMO at the University of Freiburg (DFG grant INST 39/963-1 FUGG) and the BlueCrab cluster at the Maryland Advanced Research Computing Center (MARCC).

#### References

- [1] B. J. R. Ciavarella M., Demelio G., J. Y. Hoon, Linear elastic contact of the weierstrass profile, Proceedings of the Royal Society of London. Series A. Mathematical and Physical Sciences 456 (2000) 387–405 (2000). doi:10.1098/rspa.2000.
- [2] L. Pastewka, M. O. Robbins, Contact between rough surfaces and a criterion for macroscopic adhesion, Proceedings of the National Academy of Sciences of the USA 111 (9) (2014) 3298–3303 (2014). doi:10.1073/pnas.1320846111.
- [3] J. M. Monti, A. Sanner, L. Pastewka, Distribution of gaps and adhesive interaction between contacting rough surfaces, Tribology Letters 69 (3) (2021) 80 (2021). doi:10.1007/s11249-021-01454-6.
- [4] M. H. Müser, W. B. Dapp, R. Bugnicourt, P. Sainsot, N. Lesaffre, T. A. Lubrecht, B. N. Persson, K. Harris, A. Bennett, K. Schulze, S. Rohde, P. Ifju, W. G. Sawyer, T. Angelini, H. Ashtari Esfahani, M. Kadkhodaei, S. Akbarzadeh, J. J. Wu, G. Vorlaufer, A. Vernes, S. Solhjoo, A. I. Vakis, R. L. Jackson, Y. Xu, J. Streator, A. Rostami, D. Dini, S. Medina, G. Carbone, F. Bottiglione, L. Afferrante, J. Monti, L. Pastewka, M. O. Robbins, J. A. Greenwood, Meeting the Contact-Mechanics Challenge, Tribology Letters 65 (4) (2017). doi:10.1007/s11249-017-0900-2.
- [5] B. N. J. Persson, Capillary adhesion between elastic solids with randomly rough surfaces, Journal of Physics: Condensed Matter 20 (31) (2008) 315007 (2008). doi:10.1088/0953-8984/20/31/315007.
- [6] L. Frérot, R. Aghababaei, J.-F. Molinari, A mechanistic understanding of the wear coefficient: From single to multiple asperities contact, Journal of the Mechanics and Physics of Solids 114 (2018) 172–184 (2018). doi:10.1016/j.jmps.2018.02.015.
- [7] M. Cooper, B. Mikic, M. Yovanovich, Thermal contact conductance, International Journal of Heat and Mass Transfer 12 (3) (1969) 279–300 (1969). doi:https://doi.org/10.1016/0017-9310(69)90011-8.
- [8] G. Palasantzas, J. Barnaś, Surface-roughness fractality effects in electrical conductivity of single metallic and semiconducting films, Physical Review B 56 (1997) 7726–7731 (1997). doi:10.1103/PhysRevB.56.7726.
- W. E. Wilson, S. V. Angadi, R. L. Jackson, Electrical contact resistance considering multi-scale roughness, in: 2008 Proceedings of the 54th IEEE Holm Conference on Electrical Contacts, 2008, pp. 190-197 (2008). doi:10.1109/HOLM. 2008.ECP.43.
- [10] J. Barber, Bounds on the electrical resistance between contacting elastic rough bodies, Proceedings of the Royal Society of London. Series A. Mathematical and Physical Sciences 459 (2003) 53-66 (2003). doi:10.1098/rspa.2002.1038.
- [11] J. H. Dieterich, B. D. Kilgore, Direct observation of frictional contacts: New insights for state-dependent properties, Pure and Applied Geophysics 143 (1-3) (1994) 283–302 (1994). doi:10.1007/BF00874332.

- [12] J. H. Dieterich, B. D. Kilgore, Imaging surface contacts: Power law contact distributions and contact stresses in quartz, calcite, glass and acrylic plastic, Tectonophysics 256 (1-4) (1996) 219–239 (1996). doi:10.1016/0040-1951(95)00165-4.
- [13] J. Greenwood, J. A. and Williamson, Contact of nominally flat surfaces, Proceedings of the Royal Society of London. Series A. Mathematical and Physical Sciences 295 (1442) (1966) 300–319 (1966). doi:10.1098/rspa.1966.0242.
- [14] A. Bush, R. Gibson, T. Thomas, The elastic contact of a rough surface, Wear 35 (1) (1975) 87-111 (1975). doi: 10.1016/0043-1648(75)90145-3.
- [15] B. N. J. Persson, Theory of rubber friction and contact mechanics, Journal of Chemical Physics 115 (8) (2001) 3840–3861 (2001). doi:10.1063/1.1388626.
- [16] B. N. J. Persson, Sliding Friction, Springer Berlin Heidelberg, 2000 (2000).
- [17] B. N. Persson, Elastoplastic contact between randomly rough surfaces, Physical Review Letters 87 (11) (2001) 116101-1-116101-4 (2001). doi:10.1103/PhysRevLett.87.116101.
- [18] J. Krim, G. Palasantzas, Experimental observations of self-affine scaling and kinetic roughening at sub-micron lengthscales, International Journal of Modern Physics B 09 (06) (1995) 599–632 (1995). doi:10.1142/s0217979295000239.
- [19] B. Persson, On the fractal dimension of rough surfaces, NanoScience and Technology 31 (2015) 235-248 (2015). doi: 10.1007/978-3-319-10560-4 12.
- [20] A. Gujrati, S. R. Khanal, L. Pastewka, T. D. Jacobs, Combining TEM, AFM, and profilometry for quantitative topography characterization across all scales, ACS Applied Materials and Interfaces 10 (34) (2018) 29169–29178 (2018). doi:10.1021/ acsami.8b09899.
- [21] A. Gujrati, A. Sanner, S. R. Khanal, N. Moldovan, H. Zeng, L. Pastewka, T. D. B. Jacobs, Comprehensive topography characterization of polycrystalline diamond coatings, Surface Topography: Metrology and Properties 9 (1) (2021) 014003 (2021). doi:10.1088/2051-672x/abe71f.
- [22] B. M. Forrest, L.-H. Tang, Surface roughening in a hypercube-stacking model, Phys. Rev. Lett. 64 (1990) 1405-1408 (Mar 1990). doi:10.1103/PhysRevLett.64.1405.
  URL https://link.aps.org/doi/10.1103/PhysRevLett.64.1405
- [23] H. You, R. P. Chiarello, H. K. Kim, K. G. Vandervoort, X-ray reflectivity and scanning-tunneling-microscope study of kinetic roughening of sputter-deposited gold films during growth, Phys. Rev. Lett. 70 (1993) 2900-2903 (May 1993). doi:10.1103/PhysRevLett.70.2900. URL https://link.aps.org/doi/10.1103/PhysRevLett.70.2900
- [24] E. A. Eklund, R. Bruinsma, J. Rudnick, R. S. Williams, Submicron-scale surface roughening induced by ion bombardment, Phys. Rev. Lett. 67 (1991) 1759-1762 (Sep 1991). doi:10.1103/PhysRevLett.67.1759. URL https://link.aps.org/doi/10.1103/PhysRevLett.67.1759
- [25] A. R. Hinkle, W. G. Nöhring, R. Leute, T. Junge, L. Pastewka, The emergence of small-scale self-affine surface roughness from deformation, Science Advances 6 (7) (2020) eaax0847 (2020). arXiv:https://www.science.org/doi/pdf/10.1126/ sciadv.aax0847, doi:10.1126/sciadv.aax0847. URL https://www.science.org/doi/abs/10.1126/sciadv.aax0847
- [26] R. Pohrt, V. L. Popov, Normal contact stiffness of elastic solids with fractal rough surfaces, Physical Review Letters 108 (10) (2012) 104301 (2012). doi:10.1103/PhysRevLett.108.104301.
- [27] C. Putignano, L. Afferrante, G. Carbone, G. Demelio, The influence of the statistical properties of self-affine surfaces in elastic contacts: A numerical investigation, Journal of the Mechanics and Physics of Solids 60 (5) (2012) 973–982 (2012). doi:10.1016/j.jmps.2012.01.006.
- [28] C. Campañá, M. H. Müser, Contact mechanics of real vs. randomly rough surfaces: A Green's function molecular dynamics study, Europhysics Letters 77 (3) (2007) 38005 (2007). doi:10.1209/0295-5075/77/38005.
- [29] S. Hyun, L. Pel, J. F. Molinari, M. O. Robbins, Finite-element analysis of contact between elastic self-affine surfaces, Physical Review E 70 (2 2) (2004) 1–12 (2004). doi:10.1103/PhysRevE.70.026117.
- [30] V. A. Yastrebov, G. Anciaux, J.-F. Molinari, From infinitesimal to full contact between rough surfaces: Evolution of the contact area, International Journal of Solids and Structures 52 (2015) 83–102 (2015). doi:10.1016/j.ijsolstr.2014.09.
- [31] Y. Zhou, M. H. Müser, Effect of structural parameters on the relative contact area for ideal, anisotropic, and correlated random roughness, Frontiers in Mechanical Engineering 6 (2020) 59 (2020). doi:10.3389/fmech.2020.00059. URL https://www.frontiersin.org/article/10.3389/fmech.2020.00059
- [32] L. Pei, S. Hyun, J. Molinari, M. Robbins, Finite element modeling of elasto-plastic contact between rough surfaces, Journal of the Mechanics and Physics of Solids 53 (11) (2005) 2385–2409 (2005). doi:10.1016/j.jmps.2005.06.008.
- [33] S. Hyun, M. O. Robbins, Elastic contact between rough surfaces: Effect of roughness at large and small wavelengths, Tribology International 40 (10-12) (2007) 1413–1422 (2007). doi:10.1016/j.triboint.2007.02.003.
- [34] M. Müser, A. Wang, Contact-patch-size distribution and limits of self-affinity in contacts between randomly rough surfaces, Lubricants 6 (4) (2018) 85 (2018). doi:10.3390/lubricants6040085.
- [35] C. Campañá, M. H. Müser, M. O. Robbins, Elastic contact between self-affine surfaces: comparison of numerical stress and contact correlation functions with analytic predictions, Journal of Physics: Condensed Matter 20 (35) (2008) 354013 (2008). doi:10.1088/0953-8984/20/35/354013.
- [36] C. Campañá, Using Green's function molecular dynamics to rationalize the success of asperity models when describing the contact between self-affine surfaces, Physical Review E 78 (2) (2008) 026110 (2008). doi:10.1103/PhysRevE.78.026110.
- [37] J. Kondev, C. L. Henley, Geometrical exponents of contour loops on random Gaussian surfaces, Physical Review Letters 74 (23) (1995) 4580–4583 (1995). doi:10.1103/PhysRevLett.74.4580.
- [38] Z. Olami, R. Zeitak, Scaling of island distributions, percolation, and criticality in contour cuts through wrinkled surfaces, Physical Review Letters 76 (2) (1996) 247–250 (1996). doi:10.1103/PhysRevLett.76.247.

- [39] S. B. Ramisetti, C. Campañá, G. Anciaux, J.-F. Molinari, M. H. Müser, M. O. Robbins, The autocorrelation function for island areas on self-affine surfaces, Journal of Physics: Condensed Matter 23 (21) (2011). doi:10.1088/0953-8984/23/ 21/215004.
- [40] V. A. Yastrebov, G. Anciaux, J.-F. Molinari, Contact between representative rough surfaces, Physical Review E 86 (2012) 035601 (2012). doi:10.1103/PhysRevE.86.035601.
- [41] L. Pastewka, M. O. Robbins, Contact area of rough spheres: Large scale simulations and simple scaling laws, Applied Physics Letters 108 (22) (2016). doi:10.1063/1.4950802.
- [42] K. L. Johnson, Contact Mechanics, Cambridge University Press, 1985 (1985). doi:10.1017/CB09781139171731.
- [43] C. L. Amba-Rao, Fourier transform methods in elasticity problems and an application, Journal of the Franklin Institute 287 (2) (1969) 241–249 (1969). doi:10.1016/0016-0032(69)90100-8.
- [44] H. M. Stanley, T. Kato, An FFT-based method for rough surface contact, Journal of Tribology 119 (3) (1997) 481–485 (1997). doi:10.1115/1.2833523.
- [45] I. Polonsky, L. Keer, A numerical method for solving rough contact problems based on the multi-level multi-summation and conjugate gradient techniques, Wear 231 (2) (1999) 206–219 (1999). doi:10.1016/S0043-1648(99)00113-1.
- [46] C. Campañá, M. H. Müser, Practical Green's function approach to the simulation of elastic semi-infinite solids, Physical Review B 74 (7) (2006) 075420 (2006). doi:10.1103/PhysRevB.74.075420.
- [47] L. Pastewka, T. A. Sharp, M. O. Robbins, Seamless elastic boundaries for atomistic calculations, Physical Review B 86 (7) (2012) 075459 (2012). doi:10.1103/PhysRevB.86.075459.
- [48] J. M. Monti, L. Pastewka, M. O. Robbins, Green's function method for dynamic contact calculations, Physical Review E 103 (2021) 053305 (2021). doi:10.1103/PhysRevE.103.053305.
- [49] V. A. Yastrebov, G. Anciaux, J.-F. Molinari, On the accurate computation of the true contact-area in mechanical contact of random rough surfaces, Tribology International 114 (December 2016) (2017) 161–171 (2017). doi:10.1016/j.triboint. 2017.04.023
- [50] V. A. Yastrebov, G. Anciaux, J.-F. Molinari, The role of the roughness spectral breadth in elastic contact of rough surfaces, Journal of the Mechanics and Physics of Solids 107 (2017) 469–493 (2017). doi:10.1016/j.jmps.2017.07.016.
- [51] P. Nayak, Random process model of rough surfaces, Journal of Lubrication Technology 93 (1971). doi:10.1115/1.3451608.
- 52] D. Stauffer, A. Aharony, Introduction to Percolation Theory, Taylor & Francis, 1992 (1992).
- [53] W. B. Dapp, A. Lücke, B. N. Persson, M. H. Müser, Self-affine elastic contacts: Percolation and leakage, Physical Review Letters 108 (24) (2012) 1–4 (2012). doi:10.1103/PhysRevLett.108.244301.
- [54] K. Johnson, J. Greenwood, J. Higginson, The contact of elastic regular wavy surfaces, International Journal of Mechanical Sciences 27 (6) (1985) 383 396 (1985). doi:https://doi.org/10.1016/0020-7403(85)90029-3.
- [55] V. A. Yastrebov, G. Anciaux, J.-F. Molinari, The contact of elastic regular wavy surfaces revisited, Tribology Letters 56 (1) (2014) 171–183 (2014). doi:10.1007/s11249-014-0395-z.
- [56] P. Meakin, Fractals, Scaling and Growth Far from Equilibrium, Cambridge University Press, 1998 (1998).
- [57] B. Derjaguin, V. Muller, Y. Toporov, Effect of contact deformations on the adhesion of particles, Journal of Colloid and Interface Science 53 (2) (1975) 314–326 (1975). doi:10.1016/0021-9797(75)90018-1.